

Twisted bilayer zigzag-graphene nanoribbon junctions with tunable edge states

Dongfei Wang^{1,*}, De-Liang Bao^{1,*}, Qi Zheng¹, Chang-Tian Wang¹, Shiyong Wang², Peng Fan¹, Shantanu Mishra², Lei Tao¹, Yao Xiao¹, Li Huang¹, Xinliang Feng^{3,4}, Klaus Müllen⁵, Yu-Yang Zhang¹, Roman Fasel², Pascal Ruffieux² ✉, Shixuan Du¹ ✉, and Hong-Jun Gao¹ ✉

¹*Institute of Physics & University of Chinese Academy of Sciences, Beijing 100190, China.*

²*Nanotech@surfaces Laboratory, Empa, Swiss Federal Laboratories for Materials Science and Technology, Dübendorf, Switzerland.*

³*Center for Advancing Electronics Dresden (cfaed) and Faculty of Chemistry and Food Chemistry, Technische Universität Dresden, 01062 Dresden, Germany*

⁴*Max Planck Institute of Microstructure Physics, Weinberg 2, 06120 Halle, Germany*

⁵*Max Planck Institute for Polymer Research, 55128, Mainz, Germany*

**These authors contributed equally: Dongfei Wang, De-Liang Bao.*

✉e-mail: pascal.ruffieux@empa.ch; sxdu@iphy.ac.cn; hjgao@iphy.ac.cn

Abstract

Stacking two-dimensional layered materials such as graphene and transitional metal dichalcogenides with nonzero interlayer twist angles has recently become attractive because of the emergence of novel physical properties. Stacking of one-dimensional nanomaterials offers the lateral stacking offset as an additional parameter for modulating the resulting material properties. Here, we report that the edge states of twisted bilayer zigzag-graphene nanoribbons (TBZGNRs) can be tuned with both the twist angle and the stacking offset. Strong edge state variations in the stacking region are first revealed by density functional theory (DFT) calculations. We construct and characterize twisted bilayer zigzag graphene nanoribbon (TBZGNR) systems on a Au(111) surface using scanning tunneling microscopy. A detailed analysis of three prototypical orthogonal TBZGNR junctions exhibiting different stacking offsets by means of scanning tunneling spectroscopy reveals emergent near-zero-energy states. From a comparison with DFT calculations, we conclude that the emergent edge states originate from the formation of flat bands whose energy and spin degeneracy are highly tunable with the stacking offset. Our work highlights fundamental differences between 2D and 1D twistrionics and spurs further investigation of twisted one-dimensional systems.

Keywords: edge state, zigzag graphene nanoribbon, twisted bilayer, STM/STS, van-Hove singularity.

Introduction

Monolayer graphene is a zero-energy gap semimetal hosting effective massless Dirac fermions¹. Recently, bilayer graphene with a twist angle near 1° has drawn much research attention because novel electronic ground states appear, i.e., a Mott insulating phase and superconductivity²⁻⁸. Electrons cannot move as freely as those in monolayer graphene due to the moiré potential and become strongly correlated. As a result, flat bands are formed near the Fermi energy. In tunnelling experiments, the flat bands reveal themselves as differential conductance peaks with near-zero energy⁹⁻¹². However, this is not the first time that researchers have observed flat bands in graphene systems. For example, the electrons at the edge of zigzag graphene nanoribbons (ZGNRs) become strongly correlated when the width of the ribbon decreases¹³⁻¹⁶. As a result, energy bands with little dispersion emerge in the range of $2\pi/3 \leq |\mathbf{k}| \leq \pi$ in reciprocal space (the wavenumber \mathbf{k} is normalized by the primitive translation vector of the ZGNR)¹⁷⁻²⁰, corresponding to the edge states of the ZGNR. Manipulation of such edge states with tailored properties, such as antiferromagnetic semiconductor to ferromagnetic half-metal transition²⁰, spin-splitting of dopant edge states²¹ and topological order²², is a long-lasting interesting topic with potential applications in nanodevices, i.e. spintronics^{23,24} and quantum bits²⁵. One of the methods used to tune the edge states involves stacking of one ZGNR on top of another in a parallel way. There, the energy gaps between the flat bands can be modulated with different sublattices matching up²⁶⁻³⁰. Recently, specially cut-off edges of twist bilayer graphene have been revealed to host inhomogeneous edge states³¹⁻³³. Moreover, crossed GNRs are theoretically predicted to be beam splitters and electron mirrors when integrated into nanodevices³⁴⁻³⁶. All of the above results suggest new possibilities for tuning the ZGNR edge states in a bilayer case. However, pioneering experimental and theoretical research demonstrating the tunability of the edge state with both the twist angle and stacking offset is still missing.

In this paper, we demonstrate that the edge states of twisted bilayer zigzag-graphene nanoribbons (TBZGNRs) are highly tunable from both theoretical and

experimental perspectives. First, modelling TBZGNR junctions with two 6-ZGNRs (the width of the ZGNR is 6 carbon atom chains) and density-functional-theory (DFT) calculations reveal that the edge states can be tuned over a wide range by changing not only the twist angles but also the in-plane stacking offset. Second, TBZGNR junctions were constructed with twist angle θ well controlled by STM tip lateral manipulation (with accuracy less than 5° and θ between 30° and 90°). Spatially resolved scanning tunnelling spectroscopy (STS) on several edges of the orthogonal TBZGNR junctions revealed two main features: 1) a reduction in the energy gap compared to that of monolayer ZGNR, and 2) emergent near-zero-energy peaks at the edges. Additional detailed DFT calculations were performed on several TBZGNR models with $\theta=90^\circ$. The results showed that the emergent peaks are attributable to the formation of near-zero-energy flat bands located at the edge of the stacking area due to the interlayer interaction. Moreover, the spin degeneracy of these flat bands is highly tunable with the in-plane stacking offset, which dominates the stacking symmetry. Additional calculations suggested that the out-of-plane stacking offset (interlayer distance), whose change affects the interlayer electrostatic potential and edge spin distribution, is another parameter with which to manipulate the overlapping edge states.

Results

Tunability of edge states revealed by DFT calculations

The edge states of monolayer ZGNRs manifest themselves as dispersionless bands and present as van-Hove singularities (VHS) in the calculated density of states (DOS) (peaks of the grey shadow in Fig. 1b-e). A band gap close to the Fermi energy develops due to enhanced electron-electron interactions in finite one-dimensional (1D) geometry¹³. By placing one ribbon on top of the other, as illustrated in Fig. 1a and f, the edge states are affected largely by different twist angles and in-plane stacking offsets. When the twist angle $\theta=0^\circ$ (parallel), two layers of ZGNRs typically exhibit AA or AB stacking. For AA stacking, hybridization between edge states of the top and bottom ribbons is maximized, leading to a strong edge electron hopping between the ribbons. A DFT-calculated projected density of states (PDOS) on the

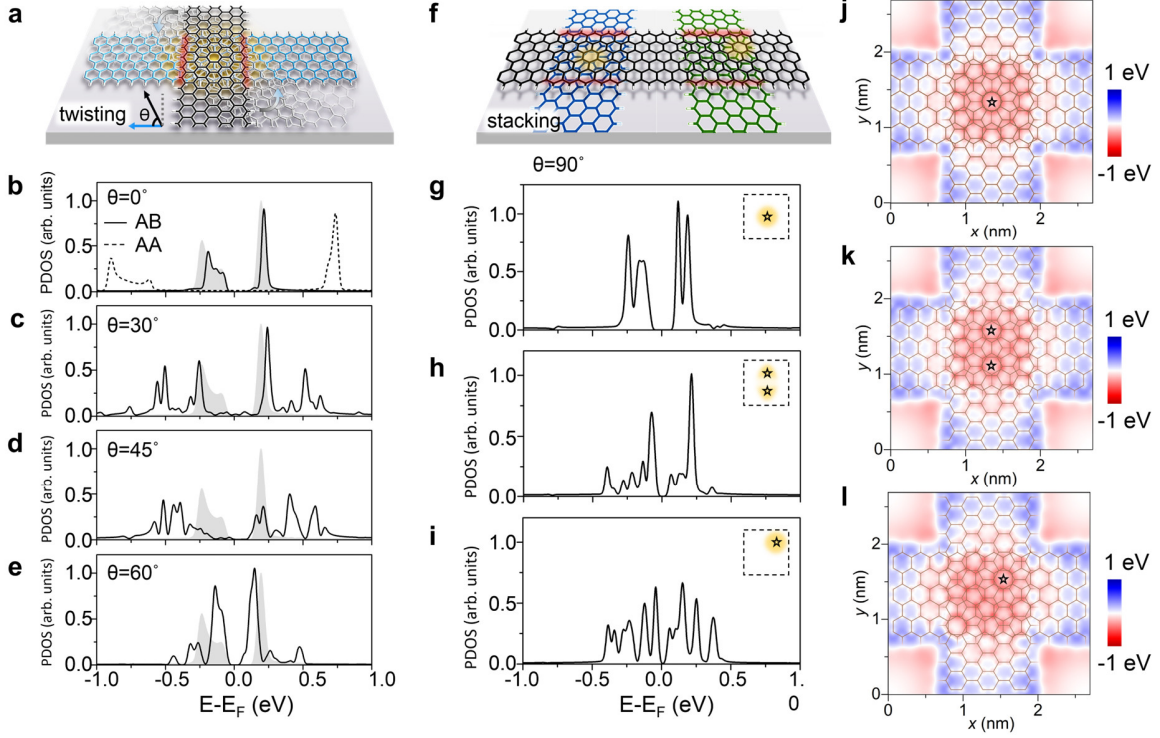


Fig. 1. | Tunability of zigzag graphene nanoribbon (ZGNR) edge states with twist angles and in-plane stacking offsets. **a**, Schematic of twisted bilayer zigzag graphene nanoribbon (TBZGNR) junctions with varying twist angles. Blue and black ribbons represent bottom and top layer ZGNRs, respectively (also in **(f)**). The angle θ represents the twist angle between the top and the bottom ribbon. Red shadow regions illustrate the edges of the top layer ZGNR within the overlapping region (also in **(f)**). **b-e**, Density-functional theory (DFT)-calculated projected density of states (PDOS) on the edge atoms in the red shadow regions in cases with several typical twist angles. In the case of a twist angle of 0° , both β -AB (solid curve) and AA stacking (dashed curve) are considered. The grey shading represents the PDOS for edge atoms in monolayer ZGNR. The results in **(c-e)** are based on structures with overlapping central hexagons, which are the most symmetric junctions. **f**, Schematic of TBZGNR junctions with the same twist angle of 90° but different in-plane stacking offsets. Two typical stacking geometries are shown here for example. The yellow shadows highlight the moiré sites with AA stacking used for distinguishing different stacking configurations. **g-i**, DFT-calculated PDOS of the edge atoms (within the red shadowed regions shown in **(f)**) in three typical TBZGNR stacking symmetries with the same twist angle of 90° . Insets show where the moiré sites are located. **j-l**, DFT-calculated interlayer electrostatic potential (in the middle plane between the top and bottom GNRs) of three 90° -TBZGNRs with the atomic stackings shown in **(g-i)**. Here the interlayer distance is fixed at 3.0 \AA for the calculation.

edges of AA-stacking bilayer ZGNRs showed that the rearranged flat bands were also revealed as VHS but with a relatively larger energy gap than the monolayer case (dashed curve in Fig. 1b). In contrast, when the two ribbons achieved AB stacking, the edge states of the top and bottom ZGNRs fell in a hybridization-avoiding geometry. The flat bands barely changed²⁶, while the gap between them was reduced slightly (solid curve in Fig. 1b). In addition to parallel AA and AB stacking, one can

also stack ZGNRs with an arbitrary twist angle θ and form a TBZGNR junction, as illustrated in Fig. 1a. Figure 1c-e clearly show that the edge states (solid curve, shown as VHS in PDOS) of TBZGNR junctions shift towards zero energy with an increasing twist angle θ when the moiré site locates at the junction center.

It is noteworthy that for a given single twist angle, there remains a rich diversity of twist symmetries tuned by the in-plane stacking offset. This is in marked contrast to two-dimensional (2D) materials in which the twist angle alone entirely defines the moiré unit cell and hence the full stacking geometry. In relation to this, the additional in-plane stacking offset used to define the geometry of the TBZGNR can be regarded as an offset vector defining the portion of the 2D moiré unit cell describing the finite overlap area and edge segments of twisted 1D structures. As an illustrative example, a TBZGNR junction with $\theta=90^\circ$ (Fig. 1f) can adopt either high (left) or low (right) stacking symmetry, whereby the edge states of junctions with different symmetries show significant changes (Fig. 1g-i). Furthermore, a reduction in the stacking symmetry directly reduces the symmetry of the interlayer electrostatic potential, as shown in Fig. 1j-l. Since a lateral external electric field was predicted to alter the spin-polarized edge states of ZGNRs²⁰, the stacking offset-dependent electrostatic potential could be the factor altering the edge states in those $\theta=90^\circ$ junctions. Calculated PDOS on edge atoms in narrower 4-ZGNRs and wider 8-ZGNRs are shown in Supplementary Figure 13 suggesting that the wider ZGNRs will produce more complicated overlapped configurations and more abundant edge states. Following the theoretical predictions described above, we built experimental TBZGNR junctions and took corresponding measurements as discussed in the following sections.

Fabrication of TBZGNRs junction with peculiar edge state

High-quality monolayer 6-ZGNRs were synthesized on Au (111) via a bottom-up method³⁷ (Fig. 2a, also see the Methods section and Supplementary Figure 1). It is challenging to build a TBZGNR junction directly with vertical STM tip manipulation. However, we noticed that the ribbon could easily be moved or even bent³⁸ on the Au surface with the STM tip (Supplementary Figure 2). Thus, we built the junction by

pushing one ribbon on top of another, which was near the step edge on the lower terrace. This idea is illustrated in Fig. 2b-c, in which a TBZGNR junction is formed with a twist angle θ . The twist angle can be controlled during manipulation. We succeeded in building TBZGNR junctions with different twist angles θ , as shown in Fig. 2d-f and Supplementary Figure 3. The decoupling effect of the bottom ZGNR makes the edge states of the top ZGNR visible

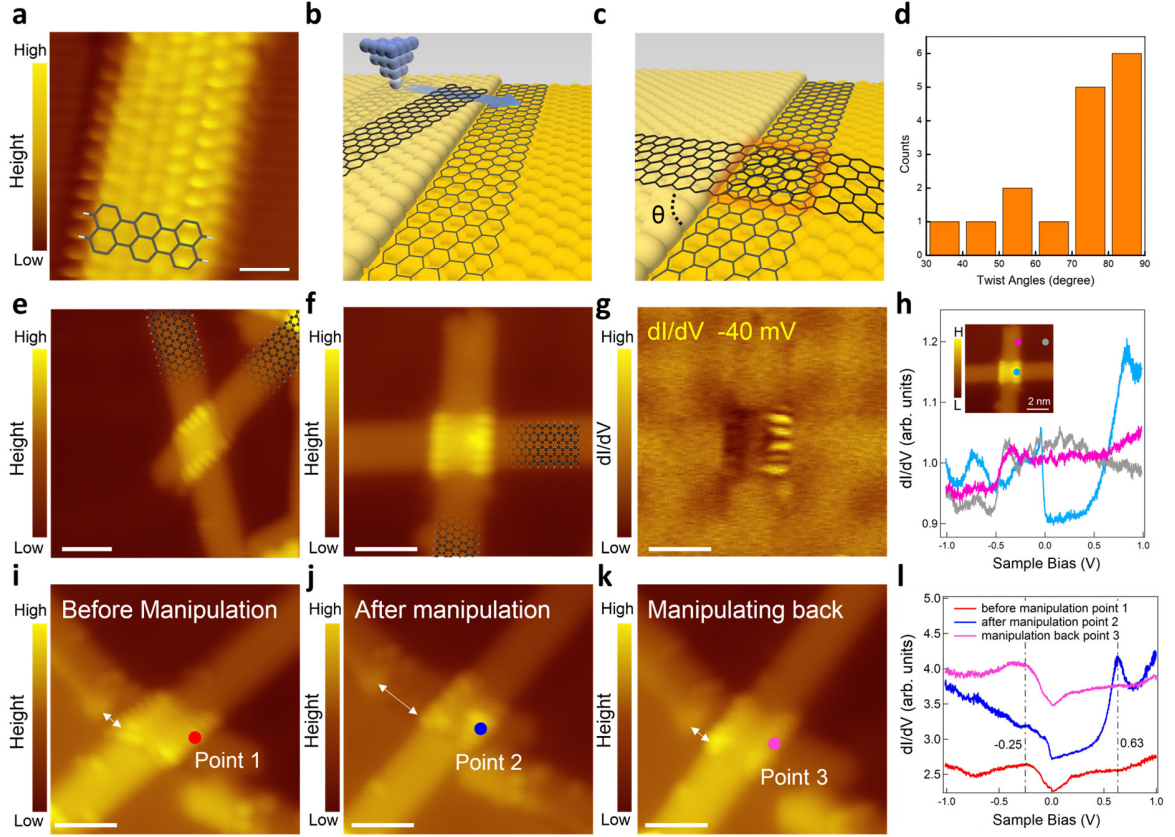


Fig. 2. | TBZGNR junctions obtained by scanning tunnelling microscopy (STM) lateral tip manipulation. **a**, High resolution STM topography image of the as-grown monolayer ZGNR. **b-c**, Schematic diagrams of ZGNRs near a step edge before and after STM tip manipulation, respectively. **d**, A histogram showing experimentally achieved twist angles θ between the top and bottom ZGNRs. **e-f**, STM topography images of two as-fabricated TBZGNR junctions with the edge states of the top ribbon clearly visualized. The twist angles of these two junctions are 53° and 87° respectively. **g**, dI/dV mapping image at -40 mV of the TBZGNR junction shown in **f**. **h**, Three typical scanning tunnelling spectroscopy (STS) measured on the junction edge (blue), on the edge of monolayer ZGNR (pink) and on the Au (111) surface (grey). Inset: Same STM topography image as **f** indicates where the STS were taken. **i-k**, Three STM topography images demonstrating the manipulation of the top ZGNR on the surface of the bottom ZGNR. The relative motion of the top ribbon is highlighted by the white arrows. **l**, Corresponding dI/dV spectra taken at points 1-3 before manipulation (red), after manipulation (blue) and manipulating the ribbon back to the initial position (pink). The vertical dashed lines highlight the change of dI/dV signals at different staking configurations. The blue and pink curves have offsets of 0.7 and 1.4 compared to the red curve for better data visualization. The blue and pink curves have offsets of 0.7 and 1.4 compared to the red curve for better data visualization. Scale bar: **(a)** 0.6 nm, **(e-g, i-k)**, 2 nm. Tunneling parameters: **(a)** $V=-0.4$ V, $I=620$ pA; **(e, i-k)** $V=-0.3$ V, $I=1.0$ nA; **(f)** $V=-93.7$ mV, $I=165$ pA; **(g, h)** $V_{\text{stab}}=-0.32$ V, $I_{\text{stab}}=1.0$ nA. $V_{\text{osc}}=0.5$ mV; **(l)** $V_{\text{stab}}=-0.3$ V, $I_{\text{stab}}=1.0$ nA. $V_{\text{osc}}=0.7$ mV.

only in the overlap region. From Fig. 2h, one can see that the STS at the edge of the monolayer ZGNR still mimics the line shape of Au (111), but the DOS at the edge of the bilayer junction changes considerably and exhibits a pronounced peak near zero

energy. The corresponding dI/dV mapping image shown in Fig. 2g clearly revealed that this near-zero-energy peak was only localized at the TBZGNR junction edge. Once TBZGNR junctions were built, further manipulations on the top ribbon can still be achieved in both directions relative to the bottom ribbon, as demonstrated in Fig. 2i-l.

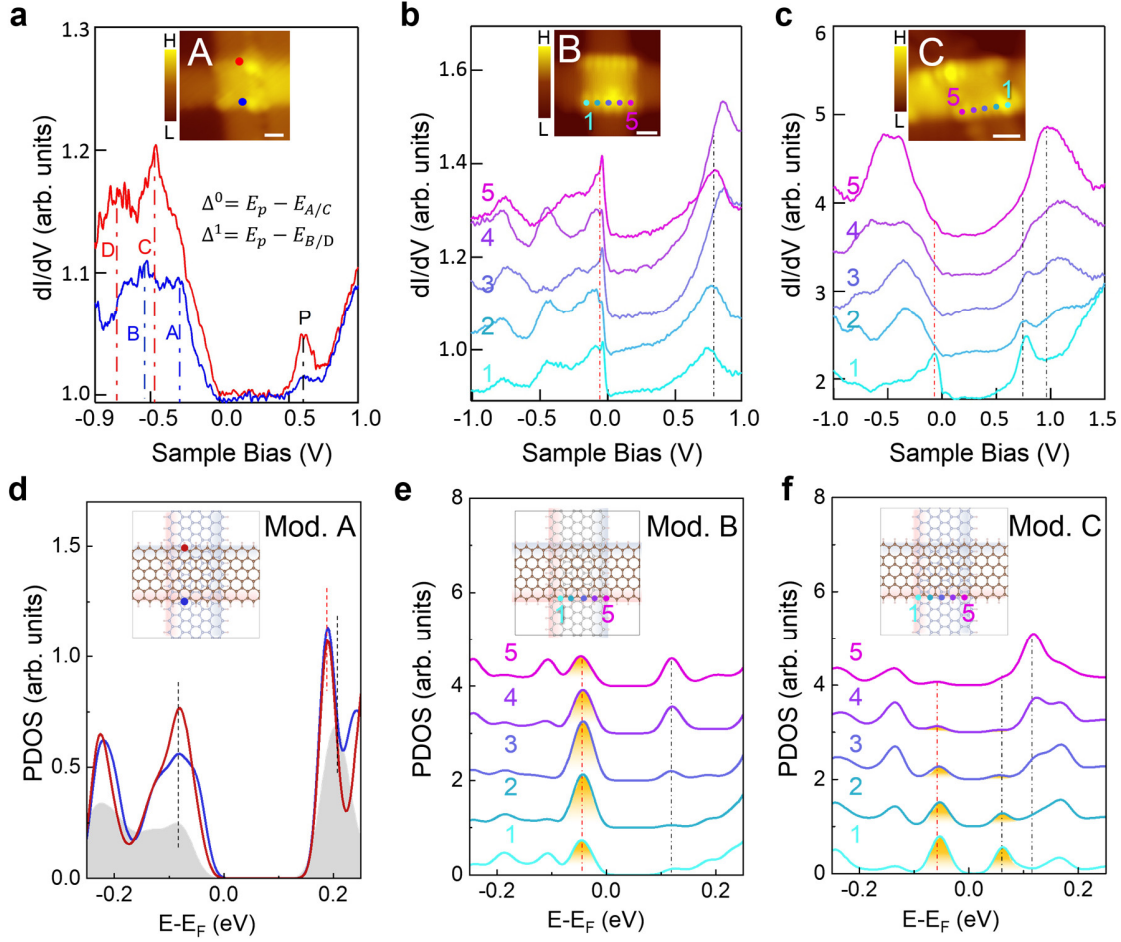


Fig. 3. | Experimental and DFT calculated results of the edge states of 3 TBZGNR junctions with $\theta \approx 90^\circ$. **a-c**, STS taken at the zigzag edges of three TBZGNR junctions. Insets in **a-c** are the STM images of the three junctions indicating where the STS were taken. Scale bar in insets: **a**, 0.7 nm, **b**, 0.76 nm, **c**, 0.74 nm. The dI/dV signals only show a gap-like feature at the edge of junction A, while a pronounced peak near zero energy was shown in TBZGNR junctions B and C (as indicated by the red vertical dashed lines). The pronounced peak near zero energy distributed along the whole bottom edge of the TBZGNR junction B, as shown in **(b)** while distributed only in the vicinity of the corner of junction C, as shown in **(c)**. The black vertical dashed lines highlight the STS peak positions above zero energy. **d-f**, DFT calculated PDOS for the edge atoms of the three TBZGNR Models A, B and C. The red and blue curves in **(d)** are the PDOS at the red and blue points shown in the inset. The grey shaded area represents the PDOS of the edge atoms in monolayer ZGNR. The curves labelled 1-5 in **(e, f)** are the PDOS for corresponding atoms 1-5 in the inset for Model B and Model C, respectively. The yellow-shaded areas highlight the PDOS peaks near zero energy. The red and black dashed lines indicate the peak energy position below and above zero energy correspondingly. The ribbon lying horizontally stands for the “top” ribbon in **(d-f)**. All models were structurally relaxed. The interlayer distances were optimized to be ~ 3 Å. Tunnelling parameters: **(a)** $V_{\text{stab}} = -0.3$ V, $I_{\text{stab}} = 1.1$ nA, $V_{\text{osc}} = 0.5$ mV; **(b)** $V_{\text{stab}} = -0.3$ V, $I_{\text{stab}} = 1.0$ nA, $V_{\text{osc}} = 0.5$ mV; **(c)** $V_{\text{stab}} = -0.3$ V, $I_{\text{stab}} = 1.0$ nA, $V_{\text{osc}} = 0.7$ mV.

To obtain more information regarding the edge states of the top layer ZGNR

within the junction, we took the spatially resolved STS at the edges. Three typical spectra recorded at the edges of TBZGNR junctions named A, B and C, and with similar $\theta \approx 90^\circ$, are shown in Fig. 3a-c, respectively (see STS data for the other twist angles in Supplementary Figure 6). From Fig. 3a, we determined that the lower edge gave energy gap values of $\Delta^0 = 0.90$ eV and $\Delta^1 = 1.15$ eV (Δ^0 and Δ^1 denote the direct band gap and the energy gap at the Brillouin zone boundary¹³), while the upper edge gave similar gap values of $\Delta^0 = 1.07$ eV and $\Delta^1 = 1.34$ eV. Compared to the gap values³⁷ for the same type of ZGNR decoupled by a NaCl layer, $\Delta^0 = 1.5$ eV and $\Delta^1 = 1.9$ eV, the band gap in our case has diminished considerably. We attribute this band gap reduction to the energy bands renormalization mainly caused by the interlayer electron hopping-induced charge redistribution between the two ZGNR layers, which did not occur when the ribbon was decoupled by a NaCl layer. DFT calculations showed that in the overlapped region of TBZGNR, electrons tended to accumulate at the interface (Supplementary Figure 4). As a result, the electron charge density at the ribbon edges was reduced, as was the corresponding effective Coulomb repulsion. The band gap reduction was proven by DFT calculations for structure Model A, as shown in Fig. 3d (see Fig. 4c for the atomic configuration). Compared to the PDOS on the edges of monolayer pristine ZGNR (grey shade), the band gaps of Model A were reduced (red and blue curves). It is worth noting that DFT calculations underestimated the band gaps, so the absolute values of the band gaps are not comparable to the experimental values. However, the relative values from the calculations are meaningful. In addition, we can't easily exclude further bandgap renormalization mechanism such as Thomas-Fermi screening when including the effect of the Au (111) surface³⁹.

Emergent near-zero-energy STS peaks were discovered at the edges of the other TNBZGNR junctions B and C (Fig. 3b and c). For junction B, the near-zero-energy peak existed along the whole edge, as indicated by the red dashed line in Fig. 3b (see also Fig. 2g). However, for junction C, this near-zero-energy peak was only found to lie near one corner of the junction (point 1) and decayed very fast to the other corner (Fig. 3c). In addition to the near-zero-energy peak, we also identified

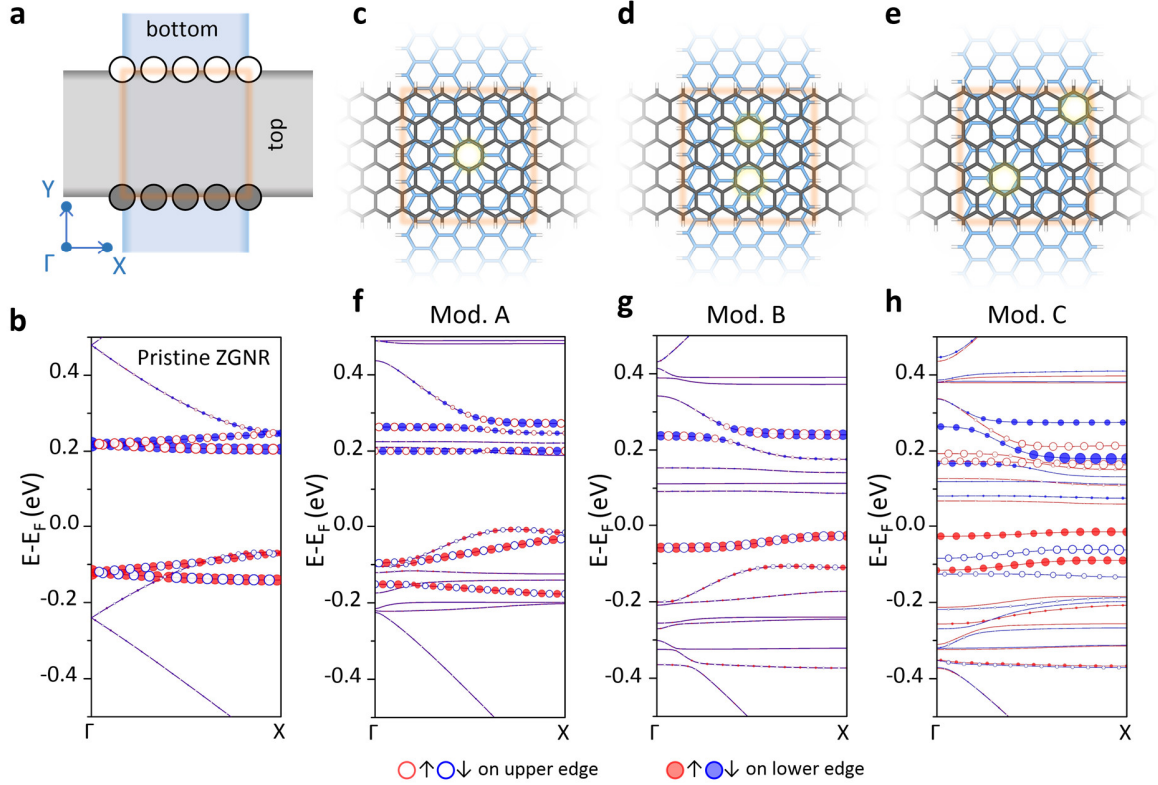


Fig. 4. | DFT calculated band structures for three designed TBZGNR models with distinct stacking symmetries. **a**, Illustration of the construction of TBZGNR models. Grey and blue ribbons represent the top and bottom ZGNRs, respectively. The light red square marks the overlapped region. The open and filled circles mark the upper- and lower-edge atoms to project on, respectively. **b**, Calculated band structures for the 11×1 -supercell monolayer of pristine ZGNR. **c-e**, atomic structures of Models A (**c**), B (**d**), and C (**e**), showing the different stacking symmetries. The structures in grey are the top ZGNRs. The light-yellow shadow highlights the moiré sites. **f-h**: Band structures calculated for Models A, B, and C, respectively. Edge-atom projections are represented as corresponding open/filled circles. Red and blue colours correspond to spin \uparrow and spin \downarrow , respectively.

other peaks at positive energies, as indicated by the black dashed lines in Fig. 3b and c. Interestingly, our DFT calculations for the other structural Models B and C, as shown in Fig. 3e and 3f correspondingly (see Fig. 4d and 4e for detailed configurations), showed results similar to those of the experiments. The PDOS shown in Fig. 3e clearly shows that in Model B, the near-zero-energy peak (indicated by the red dashed line) extended along the edge from point 1 to point 5 with a slight intensity reduction at the corner. Moreover, this peak in Model C decayed rapidly from one corner to the other (Fig. 3f). Additionally, the other calculated peaks indicated by the black dashed lines in Fig. 3e and 3f also matched the experimental data qualitatively along the edge for both junctions B and C. It is noteworthy that the

Au (111) step edges did not show any DOS anomaly near zero energy, as shown in Supplementary Figure 7, and thus did not cause additional difficulty in the corresponding analysis. Other mechanism which can cause the DOS anomaly near zero energy such as defect state can also be ruled out (Supplementary Note 8).

Manipulating the edge state by tuning stacking offsets

The primary difference among Models A, B and C is that their in-plane stacking symmetries, which are tuned by the in-plane stacking offset, reduced gradually (Fig. 4c-e). Model A has inversion, mirror, C₂, and C₆ symmetry within the overlapped region, while C₆ symmetry is absent for Model B. Finally, there is no lattice symmetry for Model C. To obtain a deeper understanding of the edge states in Models A, B and C, we calculated the full band structures of the three models first, as shown in Fig. 4f-h (solid lines). For comparison, we also calculated the band structure of a monolayer ZGNR, as shown in Fig. 4b (a justification for the calculated supercell size is presented in the Supplementary Note 7, Supplementary Figures 8 and 9). In the energy window we plotted, we identified 4 spin-degenerated bands below the Fermi energy for the monolayer ZGNR (Fig. 4b) as a result of band folding (see the Methods section). These bands were doubled to 8 but were still spin-degenerate for Models A and B because of symmetry protection (Fig. 4f and 4g). However, the bands below zero energy for Model C showed clear spin splitting (Fig. 4h), which was a direct result of the broken sublattice symmetry.

The band structures with projections on the upper and lower edges of the top ZGNR are superimposed on the full band structures (circles in Fig. 4b and Fig. 4f-h). Compared to the pristine monolayer ZGNR (Fig. 4b), we can see that the edge states (focusing on bands between -0.15 eV and 0 eV) in Model A were still spin degenerate but became more dispersive (Fig. 4f). With lower symmetry in Model B, the edge states kept the spin degeneracy but became isolated and closer to the Fermi energy (Fig. 4g), which explained the strong near-zero-energy peak in the calculated PDOS. For Model C without any symmetry, spin splitting of the edge states became evident immediately. New spin-polarized flat bands were developed close to the Fermi energy (Fig. 4h). As the time reversal symmetry was still reserved in Model C,

spin-orbital coupling⁴⁰ and pseudomagnetic field effects⁴¹⁻⁴³ did not lead to spin splitting at the Γ point. Other effects, such as Au step edge state, out-of-plane bending and lattice distortion, were also excluded (see Supplementary Notes 5 and 6, Supplementary Figures 7 and 10).

It has been indicated that an in-plane external electric field can lift the spin degeneracies of the ZGNR edge states²⁰. Considering the asymmetric stacking configuration in Model C, where the moiré site is located on the corner of the junction, the effective electron charge density showed an inhomogeneous distribution within the overlap region. Thus, an inhomogeneous electrostatic potential was introduced between the edges of the top ribbon (as shown in Fig. 1l) and played the same role as an external electric field. By extracting the potential difference within the overlapped region from Figure 1l, the estimated differential electric field is ~ 0.05 V/Å, which is comparable with that predicted in reference 20. In fact, a similar asymmetric interlayer electrostatic potential was indeed reported for crossing armchair GNRs³⁴. The symmetry-reduction-induced spin splitting in edge states was double-checked by DFT calculations based on another asymmetric TBZGNR structure, Model D (Supplementary Figure 5). It showed results consistent with those of Model C, i.e., the spin degeneracy was lifted. Based on further nc-AFM measurements on an asymmetric TBZGNR structure with twist angle 76° , the atomic structure of the junction was determined in an unambiguous way. The measured dI/dV signal across the junction also matches with the calculated PDOS using the same atomic model (Supplementary Figure 11). At this point, we concluded the in-plane stacking offset difference is the most probable factor causing different edge states for the three orthogonal TBZGNR junctions as shown in Fig. 3a-c. Twist angles other than 90° and other widths of GNRs produce longer or shorter overlapped edges, where we believe the symmetry on interlayer electrostatic potential still affects the edge states. However, the quantitatively calculational and experimental measurements need further explorations.

It is noteworthy that the interlayer electrostatic potential was sensitive to the distance between the two layers of TBZGNRs. As shown in Fig. 5a, when the

interlayer distance was increased to 3.5 Å and beyond, the potential was weakened rapidly. The edge states of TBZGNR junctions with non-90° twist angles still need further exploration, and two of them are shown in Supplementary Figure 6. Due to the rich array of possible stacking configurations, it will probably be very difficult to obtain systematic conclusions without knowing the atomic structure of the overlapped region.

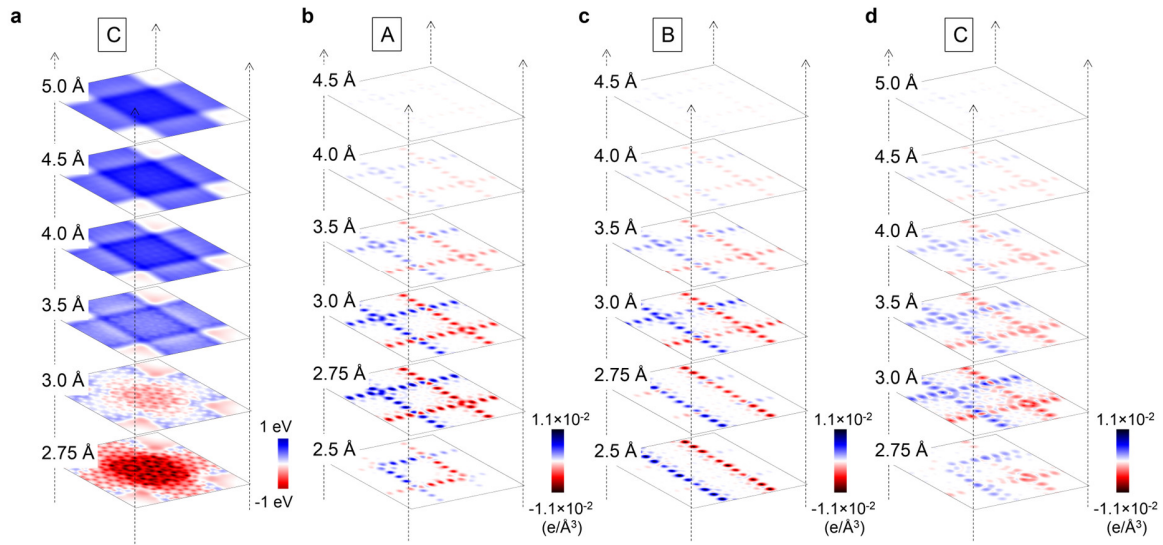


Fig. 5 | Calculated electrostatic potential distribution and spin density distribution. a, Electrostatic potential distribution in the middle plane between TBZGNRs as a function of interlayer distance (based on Model C). Blue and red colours correspond to positive and negative values, respectively. **b-d,** Spin density distribution in the middle plane between bilayer twist ZGNR as a function of interlayer distance. Blue and red represent majority spin and minority spin, respectively.

Considering the possible application of the TBZGNR network to spintronics, it is always worth knowing how the spin arrangements on the overlapping edges evolve when the interlayer distance changes (out-of-plane stacking offset). Starting from an initial antiferromagnetic order for each ZGNR, when the interlayer distances were larger than the optimal distance (~ 3.0 Å), none of the spin arrangements in any model changed, but the intensity weakened gradually (Fig. 5b-d). When the interlayer distance decreased, the spin arrangement in Model A maintained antiferromagnetic order at 2.75 Å but showed spin confinement at 2.5 Å, i.e., two

antiferromagnetic corners in the overlap region (Fig. 5b). In Model B, antiferromagnetic order of only one ZGNR was demonstrated at shorter distances (Fig. 5c). In Model C, the spin arrangement became rather asymmetric at 2.75 Å and was not localized on the edges but extended into the inside of the overlapped region at 3 Å, as displayed in Fig. 5d. The above results again emphasize the significance of stacking offset and suggest that spin frustration may exist between the two layers of TBZGNRs with short interlayer distances. Therefore, the out-of-plane stacking offset can serve as a selectable parameter for tuning the edge states of the overlapped region beyond the twist angle and in-plane stacking offset when designing a spintronic device using TBZGNRs. One possible experimental realization is fabricating TBZGNR junctions encapsulated between two insulating layers, i.e., boron nitrides. The out-of-plane stacking offset can be adjusted by tuning the insulating layers.

Discussion

We have demonstrated the presence of highly tunable edge states in the TBZGNR junction from both first-principles calculations and experiments. The featured edge states of the as-fabricated TBZGNRs combined with the reproduced theoretical results enabled us to elucidate the dominant role of stacking offsets on the edge states of TBZGNRs. Our results revealed that in twisted bilayer 1D systems, in addition to the twist angle, which is the prime factor in the 2D case, the stacking offset is another important parameter influencing the edge states as well as the charge and spin distributions of the junctions. The as-investigated 1D twisted junctions are foreseen to be construction units for nano devices, such as spin filters^{23,36,44}. Our discovery also offers intriguing opportunities for explorations on 1D twisted junctions based on materials with more abundant electronic, optical, and topological properties.

Methods

Density functional theory calculations:

DFT calculations were performed using the Vienna ab initio simulation package (VASP)^{45,46} code with the projector augmented wave (PAW)⁴⁷ method. The local spin density approximation (LSDA)⁴⁸ of Perdew-Zunger was adopted for the exchange-correlation functional. The energy cut-off of the plane-wave basis sets was 400 eV. The computational models comprised a 2.69 nm × 2.69 nm × 2 nm unit cell containing two overlapping ZGNRs with twist angles of 90°. The calculations of monolayer ZGNR used a unit cell of the same size but with only one layer of ZGNR. The numbers of carbon rings in widths/lengths of all ZGNRs were 6/11. The thickness of the vacuum layer was ~1.7 nm. The Brillouin zone was sampled with only the Γ -point. During structural relaxation, all atoms were relaxed until the force on each atom was less than 0.01 eV/Å. For the PDOS calculations, we used a 40×1×1 k mesh, where 40 was along the direction of the ZGNR that was projected on.

STM/STS manipulation and characterization:

All STM/STS measurements were performed in ultrahigh vacuum at a temperature of 4.4 K. Before switching off the feedback loop to record the differential tunnelling conductance (dI/dV) spectra, the tip was stabilized at a current (I_{stab}) and a sample bias voltage (V_{bias}). The dI/dV signal was then recorded using a lock-in technique with a bias modulation frequency of 987 Hz. Lateral STM tip manipulation of the nanoribbon was achieved via three steps. Step 1: the target GNR was located on the upper terrace of Au(111) with another GNR close to the step edge checked with STM topography images. The manipulation path, direction and position the tip were selected near the target GNR edge, which was on the opposite of the manipulation direction. Step 2: the tip was moved closer to the Au (111) surface by adjusting the current setpoint and sample bias and typical parameters such as $V=10$ mV and $I=1$ nA. The feedback loop was opened and the tip was moved along the designed path with slow speed. Step 3: the nanoribbon was checked after manipulation by scanning the target area again. If the twist angle was not what the experiment required, Steps 1 and 2 were repeated until the TBZGNR junction was fabricated.

AFM characterization:

The bond-resolved images were carried out in a Createc low-temperature STM/nc-AFM system in ultra-high vacuum (with a base pressure better than 2.0×10^{-10} mbar). The measurements were conducted at 4.5 K. A qPlus sensor (Q factor=20 000, resonant frequency=29 kHz) with Pt-Ir tip was used for STM/nc-AFM measurements. STM characterization were performed in constant current mode and the bias refer to the voltage on samples with respect to the tip. Nc-AFM data were taken with CO functionalized tip in constant height mode with oscillation amplitude of 100 pm.

Sample preparation:

Graphene nanoribbons were synthesised by following the growth protocol presented in a previous report³⁷. After precursor deposition at room temperature with the Au(111) surface held at room temperature (Supplementary Figure 1(a)), polymerization of these precursors was achieved by direct filament heating with a 2.2 A current for 10 min, and a temperature of approximately 140 °C was measured (the temperature was recorded with Optris thermometer and the emissivity was set to 0.17). These polymers were further planarized by heating again at approximately 180 °C for 10 minutes, as shown in Supplementary Figure 1(b). Most of the ribbons were synthesized on the Au terrace, with some others formed near step edges, as shown in the inset of Supplementary Figure 1(b). The width of the ribbon was approximately 1.2 nm, and the length of the ribbon was usually between 10 and 40 nm, as shown in Supplementary Figure 1(c). An atomically resolved STM topography image revealed that the monolayer ZGNR was composed of 6 zigzag carbon chains, as displayed in Fig. 2(a). Due to the itinerant *d* electron on the Au (111) surface, the intrinsic density of states of the nanoribbon was usually immersed in the Au surface state. As shown in Supplementary Figure 1(d), the *dI/dV* spectra taken at the upper and lower edges of the monolayer ZGNR (red and blue curves, respectively) showed line shapes similar to those taken on the Au (111) substrate (dashed grey curve). The reduction in the density of states near -0.5 V was due to partial screening of the Au surface state by the nanoribbon. To measure the intrinsic band structure of the nanoribbon, a less

conducting layer should be intercalated between the Au surface and the nanoribbon⁴⁹⁻⁵¹. A previous report³⁷ observed the intrinsic density of states of the zigzag edge after intercalation of a NaCl layer at the ZGNR/Au interface. However, using a STM tip to achieve vertical manipulation of the ribbon and move it onto a NaCl island is rather difficult⁵².

Data availability

Relevant data supporting the key findings of this study are available within the article and in the Supplementary Information/Source Data file. Additional data generated during the current study are available from the corresponding authors upon request.

References

- 1 Castro Neto, A. H., Guinea, F., Peres, N. M. R., Novoselov, K. S. & Geim, A. K. The electronic properties of graphene. *Rev Mod Phys* **81**, 109-162 (2009).
- 2 Bistritzer, R. & MacDonald, A. H. Moire bands in twisted double-layer graphene. *P Natl Acad Sci USA* **108**, 12233-12237 (2011).
- 3 Luican, A. *et al.* Single-Layer Behavior and Its Breakdown in Twisted Graphene Layers. *Phys Rev Lett* **106**, 126802 (2011).
- 4 Brihuega, I. *et al.* Unraveling the Intrinsic and Robust Nature of van Hove Singularities in Twisted Bilayer Graphene by Scanning Tunneling Microscopy and Theoretical Analysis. *Phys Rev Lett* **109**, 196802 (2012).
- 5 Cao, Y. *et al.* Superlattice-Induced Insulating States and Valley-Protected Orbits in Twisted Bilayer Graphene. *Phys Rev Lett* **117**, 116804 (2016).
- 6 Po, H. C., Zou, L. J., Vishwanath, A. & Senthil, T. Origin of Mott Insulating Behavior and Superconductivity in Twisted Bilayer Graphene. *Phys Rev X* **8**, 031089 (2018).
- 7 Cao, Y. *et al.* Correlated insulator behaviour at half-filling in magic-angle graphene superlattices. *Nature* **556**, 80-84 (2018).
- 8 Cao, Y. *et al.* Unconventional superconductivity in magic-angle graphene superlattices. *Nature* **556**, 43-50 (2018).
- 9 Kerelsky, A. *et al.* Maximized electron interactions at the magic angle in twisted bilayer graphene. *Nature* **572**, 95-100 (2019).
- 10 Xie, Y. L. *et al.* Spectroscopic signatures of many-body correlations in magic-angle twisted bilayer graphene. *Nature* **572**, 101-105 (2019).
- 11 Jiang, Y. H. *et al.* Charge order and broken rotational symmetry in magic-angle twisted bilayer graphene. *Nature* **573**, 91-95 (2019).
- 12 Choi, Y. *et al.* Electronic correlations in twisted bilayer graphene near the magic angle *Nat Phys* **15**, 1174 (2019).
- 13 Yang, L., Park, C. H., Son, Y. W., Cohen, M. L. & Louie, S. G. Quasiparticle energies and band gaps in graphene nanoribbons. *Phys Rev Lett* **99**, 186801 (2007).
- 14 Han, M. Y., Ozyilmaz, B., Zhang, Y. B. & Kim, P. Energy band-gap engineering of

- graphene nanoribbons. *Phys Rev Lett* **98**, 206805 (2007).
- 15 Tao, C. G. *et al.* Spatially resolving edge states of chiral graphene nanoribbons. *Nat Phys* **7**, 616-620 (2011).
- 16 Wang, S. Y. *et al.* Giant edge state splitting at atomically precise graphene zigzag edges. *Nat Commun* **7**, 11507 (2016).
- 17 Fujita, M., Wakabayashi, K., Nakada, K. & Kusakabe, K. Peculiar localized state at zigzag graphite edge. *J Phys Soc Jpn* **65**, 1920-1923 (1996).
- 18 Nakada, K., Fujita, M., Dresselhaus, G. & Dresselhaus, M. S. Edge state in graphene ribbons: Nanometer size effect and edge shape dependence. *Phys Rev B* **54**, 17954-17961 (1996).
- 19 Wakabayashi, K., Fujita, M., Ajiki, H. & Sigrist, M. Electronic and magnetic properties of nanographite ribbons. *Phys Rev B* **59**, 8271-8282 (1999).
- 20 Son, Y. W., Cohen, M. L. & Louie, S. G. Half-metallic graphene nanoribbons. *Nature* **444**, 347-349 (2006).
- 21 Blackwell, R. E. *et al.* Spin splitting of dopant edge state in magnetic zigzag graphene nanoribbons. *Nature* **600**, 647-652 (2021).
- 22 Groning, O. *et al.* Engineering of robust topological quantum phases in graphene nanoribbons. *Nature* **560**, 209-213 (2018).
- 23 Ozaki, T., Nishio, K., Weng, H. & Kino, H. Dual spin filter effect in a zigzag graphene nanoribbon. *Phys Rev B* **81**, 075422 (2010).
- 24 Pesin, D. & MacDonald, A. H. Spintronics and pseudospintronics in graphene and topological insulators. *Nat Mater* **11**, 409-416 (2012).
- 25 Slota, M. *et al.* Magnetic edge states and coherent manipulation of graphene nanoribbons. *Nature* **557**, 691-695 (2018).
- 26 Sahu, B., Min, H., MacDonald, A. & Banerjee, S. K. Energy gaps, magnetism, and electric-field effects in bilayer graphene nanoribbons. *Phys Rev B* **78**, 045404 (2008).
- 27 Zhong, X., Pandey, R. & Karna, S. P. Stacking dependent electronic structure and transport in bilayer graphene nanoribbons. *Carbon* **50**, 784-790 (2012).
- 28 Fang-Ping, O., Li-Jian, C., Jin, X. & Hua, Z. Electronic properties of bilayer zigzag graphene nanoribbons: First principles study. *Chinese Physics Letters* **28**, 047304 (2011).
- 29 Miyamoto, Y., Nakada, K. & Fujita, M. First-principles study of edge states of H-terminated graphitic ribbons. *Phys Rev B* **59**, 9858 (1999).
- 30 Santos, H., Ayuela, A., Chico, L. & Artacho, E. van der Waals interaction in magnetic bilayer graphene nanoribbons. *Phys Rev B* **85**, 245430 (2012).
- 31 Morell, E. S., Vergara, R., Pacheco, M., Brey, L. & Chico, L. Electronic properties of twisted bilayer nanoribbons. *Phys Rev B* **89**, 205405 (2014).
- 32 Pelc, M., Morell, E. S., Brey, L. & Chico, L. Electronic conductance of twisted bilayer nanoribbon flakes. *The Journal of Physical Chemistry C* **119**, 10076-10084 (2015).
- 33 Wang, Z.-H. *et al.* One-dimensional topological superconductivity at the edges of twisted bilayer graphene nanoribbons. *Phys Rev B* **100**, 094531 (2019).
- 34 Brandimarte, P. *et al.* A tunable electronic beam splitter realized with crossed graphene nanoribbons. *The Journal of Chemical Physics* **146**, 092318 (2017).
- 35 Sanz, S., Brandimarte, P., Giedke, G., Sánchez-Portal, D. & Frederiksen, T. Crossed graphene nanoribbons as beam splitters and mirrors for electron quantum optics. *Phys Rev B* **102**, 035436 (2020).
- 36 Sanz, S. *et al.* Spin-Polarizing Electron Beam Splitter from Crossed Graphene Nanoribbons. *Phys Rev Lett* **129**, 037701 (2022).
- 37 Ruffieux, P. *et al.* On-surface synthesis of graphene nanoribbons with zigzag edge topology. *Nature* **531**, 489-492 (2016).
- 38 van der Lit, J., Jacobse, P. H., Vanmaekelbergh, D. & Swart, I. Bending and buckling of

- narrow armchair graphene nanoribbons via STM manipulation. *New J Phys* **17**, 053013 (2015).
- 39 Kim, M. *et al.* Control of electron-electron interaction in graphene by proximity
screening. *Nat Commun* **11**, 2339 (2020).
- 40 Kunschuh, S., Gmitra, M., Kochan, D. & Fabian, J. Theory of spin-orbit coupling in
bilayer graphene. *Phys Rev B* **85**, 115423 (2012).
- 41 Guinea, F., Katsnelson, M. I. & Geim, A. K. Energy gaps and a zero-field quantum Hall
effect in graphene by strain engineering. *Nat Phys* **6**, 30-33 (2010).
- 42 Jiang, Y. H. *et al.* Visualizing Strain-Induced Pseudomagnetic Fields in Graphene
through an hBN Magnifying Glass. *Nano Lett* **17**, 2839-2843 (2017).
- 43 Mao, J. H. *et al.* Evidence of flat bands and correlated states in buckled graphene
superlattices. *Nature* **584**, 215-220 (2020).
- 44 Martins, T. B., da Silva, A. J., Miwa, R. H. & Fazzio, A. σ - and π -Defects at graphene
nanoribbon edges: building spin filters. *Nano Lett* **8**, 2293-2298 (2008).
- 45 Kresse, G. & Furthmüller, J. Efficient iterative schemes for ab initio total-energy
calculations using a plane-wave basis set. *Phys Rev B* **54**, 11169 (1996).
- 46 Vanderbilt, D. Soft self-consistent pseudopotentials in a generalized eigenvalue
formalism. *Phys Rev B* **41**, 7892 (1990).
- 47 Kresse, G. & Joubert, D. From ultrasoft pseudopotentials to the projector augmented-
wave method. *Phys Rev B* **59**, 1758 (1999).
- 48 Perdew, J. P. & Zunger, A. Self-interaction correction to density-functional
approximations for many-electron systems. *Phys Rev B* **23**, 5048 (1981).
- 49 Deniz, O. *et al.* Revealing the Electronic Structure of Silicon Intercalated Armchair
Graphene Nanoribbons by Scanning Tunneling Spectroscopy. *Nano Lett* **17**, 2197-2203
(2017).
- 50 Deniz, O. *et al.* Electronic characterization of silicon intercalated chevron graphene
nanoribbons on Au(111). *Chem Commun* **54**, 1619-1622 (2018).
- 51 Jacobse, P. H., Mangnus, M. J. J., Zevenhuizen, S. J. M. & Swart, I. Mapping the
Conductance of Electronically Decoupled Graphene Nanoribbons. *ACS Nano* **12**, 7048-
7056 (2018).
- 52 Gigli, L. *et al.* Detachment Dynamics of Graphene Nanoribbons on Gold. *ACS Nano* **13**,
689-697 (2019).

Acknowledgements

We would like to thank Min Ouyang, Steven Louie, Sokrates T. Pantelides, and Jiebin Peng for useful discussions. H.-J. G. and S. D. gratefully acknowledge funding by National Natural Science Foundation of China (61888102). P. R. and R. F. gratefully acknowledge funding by the Swiss National Science Foundation under Grant No. IZLCZ2_170184. S. D. gratefully acknowledge funding by the Strategic Priority Research Program of Chinese Academy of Sciences (No. XDB30000000). Y.-Y. Z. gratefully acknowledge funding by the National Key Research and Development Program of China (No. 2019YFA0308500). S. D. and Y.-Y. Z. gratefully acknowledge funding by the K. C. Wong Education Foundation and the

International Partnership Program of Chinese Academy of Sciences (No. 112111KYSB20160061). D.-L. B. gratefully acknowledge funding by China Postdoctoral Science Foundation (No. 2018M641511). X. F. gratefully acknowledge funding by EU Graphene Flagship 881603 (GrapheneCore3). D.-L. B., C.-T. W., L. T., Y.-Y. Z. and S. D. gratefully acknowledge the computational resources provided by the National Supercomputing Center in Tianjin.

Author Contributions Statement

D. W. and D.-L. B. contributed equally to this work. H.-J.G. supervised the overall research. S. D., P. R., R. F. and H.-J. G. designed the experiments. D. W., P. F., S. M. and S. W. performed the scanning tunneling microscopy experiments. Q. Z., Y. X., and L. H. performed the AFM experiments. D.-L. B., C.-T. W., L. T., Y.-Y. Z. and S. D. performed the theoretical calculations. X. F. and K. M. provided the molecular precursors. D. W., D.-L. B., S. D., P. R., R. F. and H.-J. G. wrote the manuscript. All authors analysed the data and contributed to the preparation of the manuscript.

Competing Interests Statement

The authors declare no competing interests.

Supplementary information

Supplementary information is available online and includes the following:

- Supplementary Notes 1-9
- Supplementary Figures 1-13
- Supplementary References

Supplementary Information: Twisted bilayer zigzag-graphene nanoribbon junctions with tunable edge states

Dongfei Wang^{1,*}, De-Liang Bao^{1,*}, Qi Zheng¹, Chang-Tian Wang¹, Shiyong Wang², Peng Fan¹, Shantanu Mishra², Lei Tao¹, Yao Xiao¹, Li Huang¹, Xinliang Feng^{3,4}, Klaus Müllen⁵, Yu-Yang Zhang¹, Roman Fasel², Pascal Ruffieux² ✉, Shixuan Du¹ ✉, and Hong-Jun Gao¹ ✉

¹*Institute of Physics & University of Chinese Academy of Sciences, Beijing 100190, China.*

²*Nanotech@surfaces Laboratory, Empa, Swiss Federal Laboratories for Materials Science and Technology, Dübendorf, Switzerland.*

³*Center for Advancing Electronics Dresden (cfaed) and Faculty of Chemistry and Food Chemistry, Technische Universität Dresden, 01062 Dresden, Germany*

⁴*Max Planck Institute of Microstructure Physics, Weinberg 2, 06120 Halle, Germany*

⁵*Max Planck Institute for Polymer Research, 55128, Mainz, Germany*

**These authors contributed equally: Dongfei Wang, De-Liang Bao.*

✉e-mail: pascal.ruffieux@empa.ch; sxdu@iphy.ac.cn; hjgao@iphy.ac.cn

TABLE OF CONTENTS

- Supplementary Notes 1-9
- Supplementary Figures 1-13
- Supplementary References

Supplementary Notes:

1. Reversible STM Tip Manipulation of ZGNRs

It is reported that the graphene nanoribbon with armchair edge has superlubricity on gold surface¹. Here, by STM tip manipulation, we proved that the graphene nanoribbon with zigzag edge can also be easily lateral moved and manipulated on gold surface like the arm-chair case². As shown in Supplementary Figure 2(b), the ribbon was firstly bent by the STM lateral manipulation in a direction indicated by the white arrow. Then, the ribbon was bent back to its original position with tip manipulation in a reversal direction as shown in 2(c) and 2(a). Furthermore, we bent the ribbon again in the direction same with 2(b) but with a smaller bending angle as shown in 2(d). From 2(a) and 2(c) we can see the ribbon has similar quality after the bending.

2. STM images of more TBZGNR Junctions

With the STM lateral tip manipulation technique mentioned above, we can achieve TBZGNR junctions with different twist angles. 16 of them are shown in Supplementary Figure 3. The achieved twisted angles range from 30° to 90°.

3. Charge redistribution within the TBZGNR junction

Previous study on bilayer graphene³ shows the finite interlayer hopping could influence the low-energy band structure of graphene. This is also true for the case of bilayer graphene nanoribbon. The interlayer hopping manifests itself as a finite bonding between the electrons of the top and bottom ribbon. Thus, the effective electron charge redistributes in the overlapping region. By DFT calculation, this effect is clearly shown in Supplementary Figure 4 where a net electron charge accumulation happened in the space between the top and bottom ribbon.

4. DFT results for another TBZGNR structural model, Model D

In order to further verify the theory that a TBZGNR without symmetry can support spin polarized flat band at the edge as we argued in the main text and Figure 4(e), we construct another TBZGNR structure model D also without symmetry. The DFT calculated results are shown in Supplementary Figure 5. From Supplementary Figure

5(b) we can see again a pronounced peak near zero energy is developed only near the corner of the overlapped region. This peak also originates from a new flat band near zero shown in 5(c). We can further identify the bands are spin non-degenerate with a relatively small splitting energy. All these features are similar to what we obtained for the model C in the main text. Thus, our argument that the asymmetrical van de Waals potential produces spin polarized flat bands in TBZGNR is repeated in another model structure.

5. Influence of the Au (111) surface state and step edge on the spectra of monolayer ZGNR

As the ZGNR used in this work is the same as that used in the previous reference⁴, the edge only terminated with C-H bond. Because we do not intentionally make a bias pulse, the C-Au bonding reported in the other reference⁵ is also not the case. From the previous theory prediction⁶ it is shown that the ZGNR on Au (111) still displays a magnetic edge state with antiferromagnetic coupling between the edges. The magnetization per edge C atom is about 0.22 μB which is comparable to the free-standing ZGNRs. These edge states are not observed mainly due to the strong extension of the surface state of Au (111) in the out of plane direction. From the Figure 2 in previous report⁷ we can clearly see the Au (111) surface state survive even 2 Å away from the surface. The apparent height of our monolayer ZGNR is just 1.85 Å. Thus, most of the ZGNR edge states are in the shadow of the Au (111) surface state, this is also the reason why the DOS at the monolayer edge mimics the surface state of Au (111), as already seen in the Figure 2h.

Recently, an interesting work⁸ reported effective pi bonding between C and Au atoms when the ribbon edge is doped by nitrogen. However, this is not the case here as we never see an effective decoupling of the monolayer ribbon by ramping a bias sweep, also the ribbon used is not nitrogen doped.

As the bottom ribbon of the junction always lies in the vicinity of the Au (111) step edges, it is a necessary to discuss the influence of the step edges on the density of state we obtained on the TBZGNR junction. Taking one junction with a twist angle near

80° for example, the Au step edge is highlighted with a white dashed box in the STM topography image shown in Supplementary Figure 7(a). By comparing with corresponding dI/dV mapping images at energies we interested in this study, we did not find any evident density of state distribution on the Au step edges, as shown in 7(b) and 7(c). In contrast, the edge state of the top zigzag graphene nanoribbon at the junction is clearly demonstrated, as highlighted by the yellow arrows. Thus, it concludes that the step edge of the Au (111) will not give additional influence on our data analysis regarding the energies we are interested.

6. Exclusion of out-of-plane bending and lattice distortion effects

We estimate the out-of-plane bending effect of the top ZGNR by taking the line profile across the TBZGNR junction, as demonstrated in Supplementary Figure 10(a). From the results shown in 10(b) we can see that the ribbon bending angle $\theta=165.3^\circ$, which means very tiny bending and out-of-plane distortion. Our theoretical calculation also gives a similar bending angle near 177° which is even larger than the value measured from the experiment. The previous theoretical calculations indicates that when the bending angle θ range between 100° and 180° , both the AFM magnetic ground state and the energy gap are essentially the same⁹. Thus, the pure bending and out-of-plane distortion effect will not play a role in our study.

On the other hand, the lattice distortion in graphene system can also introduce some important physical effect such as pseudo-magnetic field. Compared to the previous reports where the strain mainly due to a designed structure confinement by the substrate^{10,11}, the fabrication process of TBZGNR does not introduce any additional strain, as: 1) the Au surface is flat and no substrate template effect; 2) the end of the top ribbon is free, strain due to confinement can be ignored. There are some possibilities that the Van der Waals and gravity can introduce some lattice distortion at the TBZGNR junction edge, However, from some simple calculations we can show that these two effects can also be excluded, as shown below:

We consider two extreme cases:

a) the lattice distortion only induced by the gravity of the tail part of the top GNR as illustrated in Supplementary Figure 10(c). If we assume the tail part has a length of 5 nm, in total we have 264 carbon atoms there, which has a gravity of 5.17×10^{-23} N. The

cross section at the edge of the junction is $5.1 \times 10^{-19} \text{ m}^2$ if we take the interlayer distance 0.45 nm and the width of the ribbon 1.14 nm. Therefore, the stress at the edge is $1.01 \times 10^{-4} \text{ Pa}$. Because of the Graphene's super high Young's modulus of $E = 1.0 \text{ TPa}$, the strain at the edge is 10^{-16} , which is very tiny.

b) the lattice distortion only induced by the in-plane van de Waals' pulling force of the tail part of the top GNR, as illustrated in Supplementary Figure 10(d). From previous experiment¹² we learned the shear stress of graphene on a silicon oxide surface is around 1.64 MPa, if we take the same Young's modulus 1 TPa, we get a strain of 1.64×10^{-6} , which is also very small.

It is demonstrated experimentally that 1%-2% strain in graphene can only introduce 0.7 T pseudo-magnetic field¹³. So, in our case there is no additional strain and related pseudo-magnetic field induced by both gravity and van der Waals force. This is also demonstrated in Figure 3 that no corresponding symmetric Landau Levels found in experiment and DFT calculation.

There is another evidence that the near zero energy bound state does not originate from strain effect. The dI/dV mapping image at -40 mV in main text Figure 2g shows the bound state localized at both the edges and the corners of the junction. The periodicity is the same as that of the zigzag carbon atoms, which demonstrate the near zero energy bound state is junction structure related other than strain related.

7. Exclusion of supercell size and a possible intersupercell interaction effect

The total energy per atom as a function of the lattice constant of the supercell were carefully tested in the calculation. As shown in the Supplementary Figure 8(a) and 8(b), the energy difference converges to 0.001 eV/atom from $L \approx 27 \text{ \AA}$ to 32 \AA . We chose the 27 \AA cell (11 carbon rows in length) to do all other calculations, considering the balance between calculational performance and cost. The calculated electronic structures of modeled TBZGNRs already agree well with experiments for $L \approx 27 \text{ \AA}$.

We further did a calculation on a non-periodic structure for comparison as shown in Supplementary Figure 8(c) and 8(d). From the projected density of states (PDOS) shown in 8(d) we can see the results are highly similar with that in the main text Figure 3f, which demonstrate that the featured asymmetric PDOS peaks originate from the stacking.

We also checked the PDOS at the edge of monolayer ZGNR in the vicinity of the TBZGNR junction with DFT calculation, as shown in Supplementary Figure 9. The PDOS at the monolayer ZGNR edge already demonstrating a gap like line shape, mimic that of the pristine GNR, although the corresponding carbon atom just shift 2 lattice constants from the junction corner. The featured near-zero-energy peaks observed on the edge atoms in the crossing region are obviously absent.

Thus, the possibility that the emergence of the near-zero-peak owing to the calculating size of the supercell and possible interactions between periodic supercells are excluded.

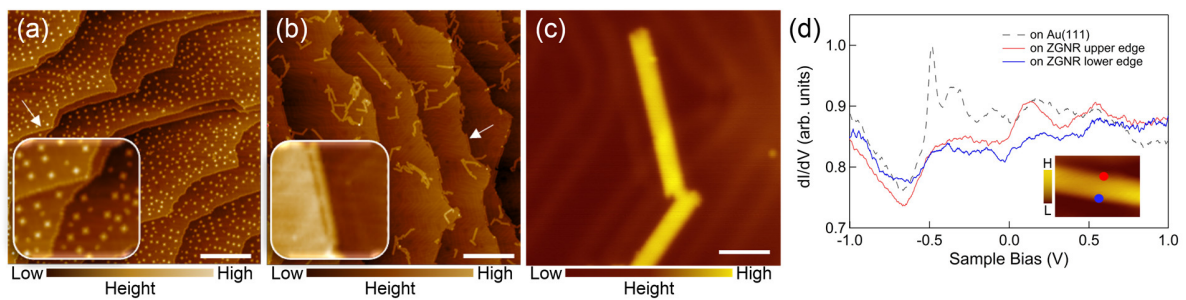
8. Exclusion of the influence of bright protrusions on the edge state

As there are some bright protrusions on Figure 2f and 2j, it is a necessary to check they has no relation with the edge states we discuss in the paper. By checking the dI/dV mapping in Fig. 2g we found no additional signal belongs to the protrusion shown in Fig. 2f at the edge state energy -40 mV. From the tip manipulation of the top ribbon shown in Fig. 2i-2k, we learned the bright feature on the right edge of top ribbon appears for the first manipulation (Fig. 2j) and disappears again (Fig. 2k) after manipulating back. As our tip is far from the junction during the manipulation, it is very unlikely to be adatom. These bright protrusions are also excluded to be “mouse-bite” type defect on the edge of the single layer ZGNR because of two facts. Firstly, the bright protrusions shown in Figs. 2f,j and Fig. 3b appear in the middle of the top ribbon edge within the junction, which means they sit on the middle of the bottom ribbon. However, the “mouse-bite” type defect appears mostly on the edge of the bottom ribbon. Secondly, as seen in Figure S4 in the supplementary information of reference 4, the STS on the “mouse-bite” type defect (indicated by red triangle) does not resemble what we have shown in Figure 3(a-c), where either clear gap feature or in-gap states were observed. Thus, we can safely exclude that the bright features in Figs. 2f,j and the insets for Fig. 3a,b are this type of defect. We propose the protrusions we observed to be a tiny stress states at the edges which, as we demonstrated already in previous section, will not lead to great impact (the top ribbon edge at the junction is still very straight and has a strain less than 1%).

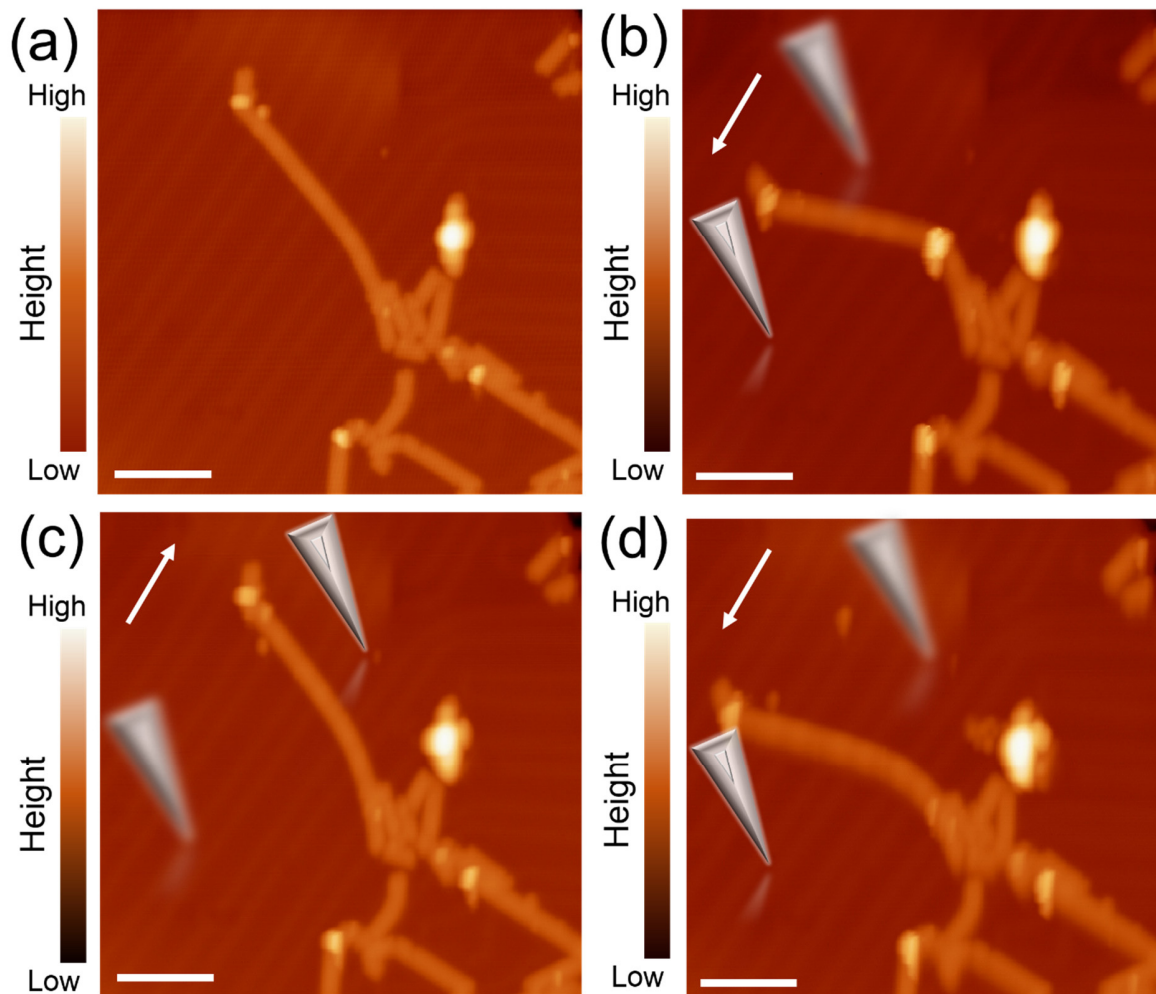
9. Nc-AFM measurements on a 76° TBZGNR junction together with DFT calculation

To unambiguously make a link between the structure of the junction and the observed edge state, we employed both STM and nc-AFM and got some initial results regarding the structure and DOS. The new junction we studied has a twist angle of 76° as shown in Supplementary Figure 11a. In order to determine the atomic structure, nc-AFM measurements were done on both the bottom and top 6-ZGNR as shown in 11b and 11c. By extending the model structures from nc-AFM measurements we resolve the atomic model of this 76° TBZGNR junction shown in 11d. By comparing the experimental dI/dV spectra (Supplementary Figure 11f) with the DFT-calculated PDOS (Supplementary Figure 11g) along a similar path across the junction, one can get good agreement between the experiment and the calculation, just like the data shown in the main text Figure 3. For example, the peaks just above the Fermi energy are strongest only at the edge, and the signal at the left edge is slightly stronger than that at the right edge, as highlighted by the red dashed lines. The relative energy positions of the peaks below the Fermi energy (highlighted by black and blue arrows) to those just above the Fermi energy (highlighted by red dashed lines) also agree qualitatively between experiment and calculation. Noteworthy, the as-constructed 76° junction also lacks inversion or mirror symmetry, so asymmetric edge states were found both by experiment and calculation. Thus, the nc-AFM measurements further support our argument in the main text and emphasize the importance of stacking offset in the determination of edge state.

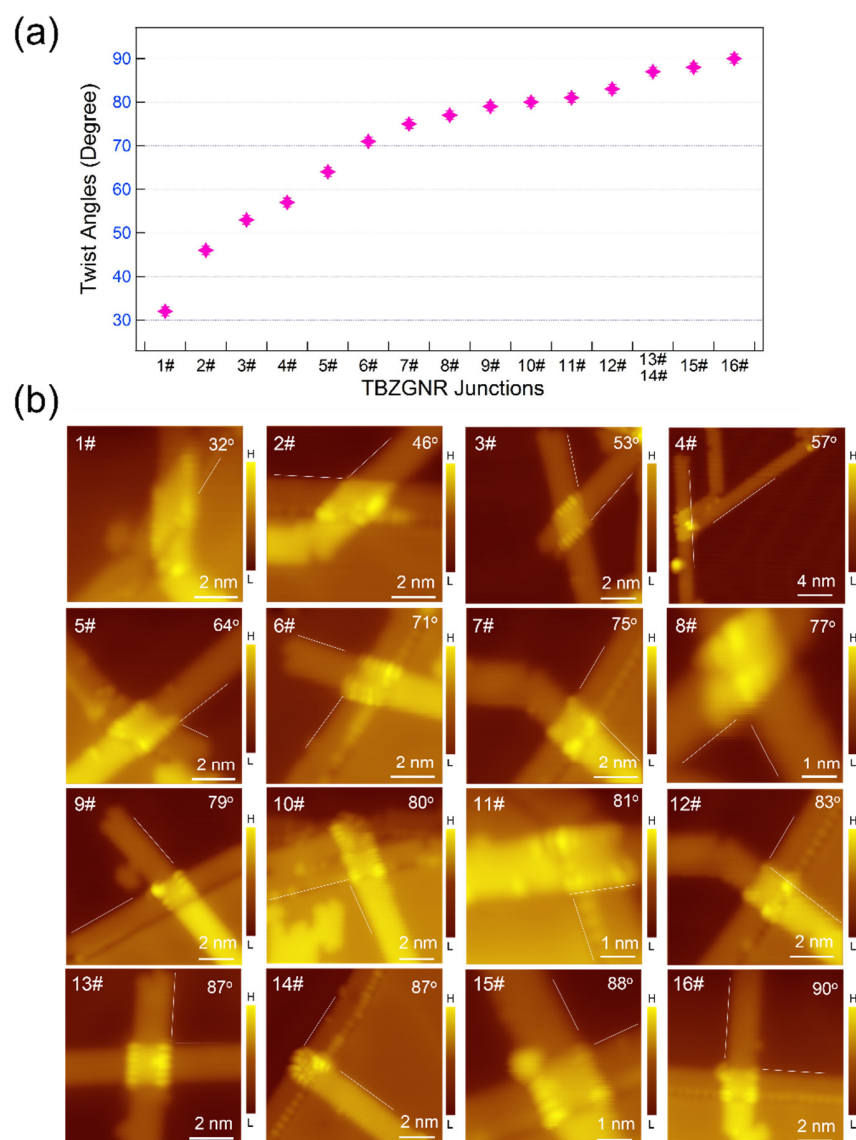
Supplementary Figures 1-13



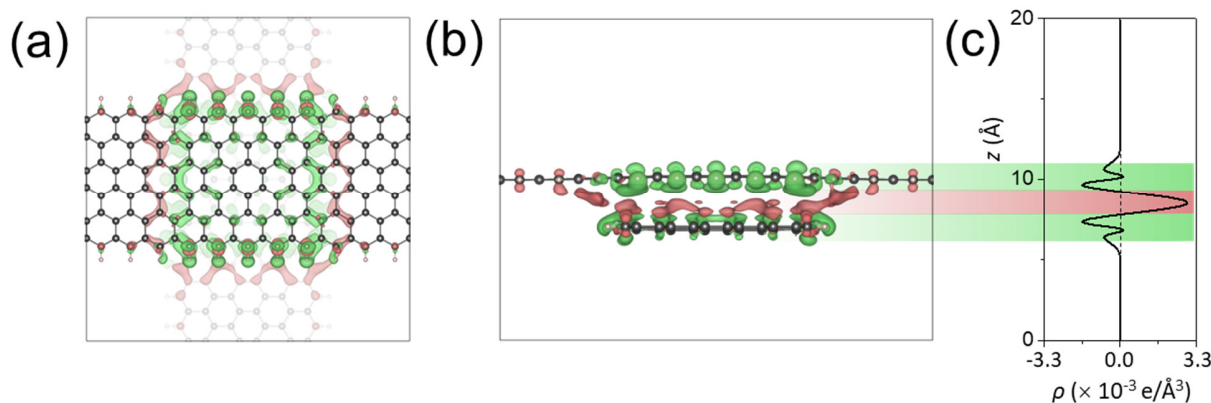
Supplementary Figure 1. Growth and characterization of individual 6-ZGNRs on Au (111). (a) STM topography image of the precursor deposition on Au (111) surface. Inset: Zoom in image of the precursor absorbed near the Au step edge. (b) STM topography image of ZGNR after annealing the pre-deposited precursors on Au (111) surface. Inset: Zoom in image of ZGNR formed near Au step edge. (c) STM topography image of the monolayer ZGNR formed on the Au terrace. (d) STS taken on the top (red) and bottom (blue) edge of the monolayer ZGNR. Grey curve shows a typical STS on the gold surface. Inset: STM topography image of a monolayer ZGNR indicating where the STS were taken, size 5.1 nm \times 3.6 nm. Scale bar: (a-b) 40 nm, (c) 4 nm. Tunneling parameters: (a-b) $V=0.5$ V, $I=50.0$ pA, (c) $V=-0.3$ V, $I=1.0$ nA; (d) $V_{\text{stab}}=-0.3$ V, $I_{\text{stab}}=1.0$ nA, $V_{\text{osc}}=0.5$ mV



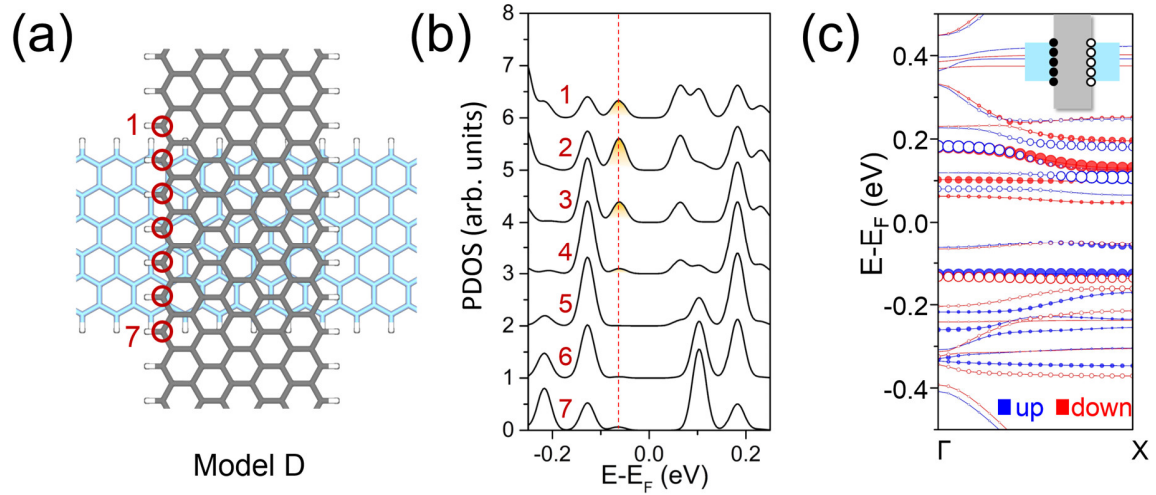
Supplementary Figure 2. Demonstration of STM tip manipulations on a monolayer ZGNR. (a-d) Reversible STM tip manipulation of ZGNR demonstrated with sequential STM topography images. The blurred and solid silver triangle illustrate the tip position before and after tip manipulation. The white arrow indicates the manipulating direction. Scale bar: (a-d) 10 nm. Tunneling parameters: (a-d) $V=-0.3$ V, $I=1.2$ nA.



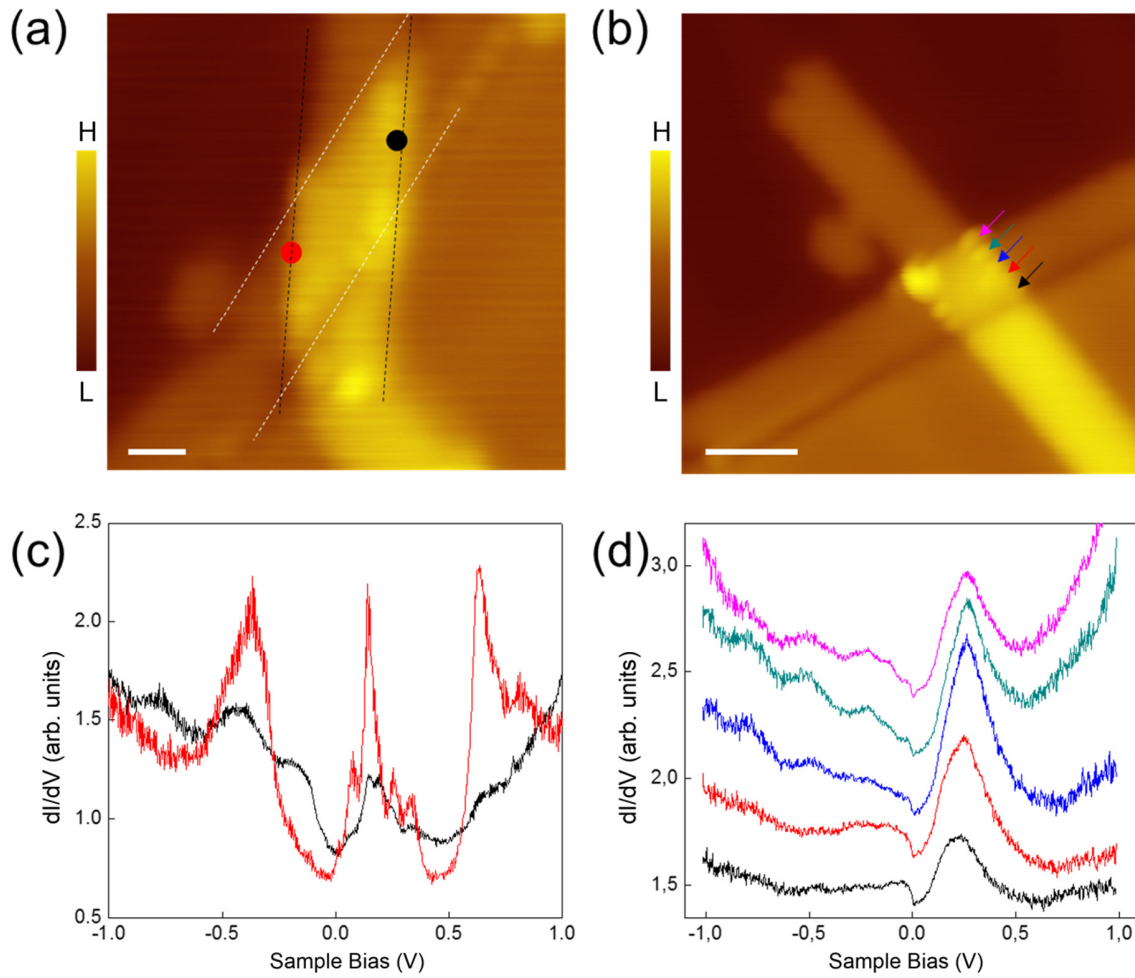
Supplementary Figure 3. 16 TBZGNR junctions prepared in this study. (a) The twist angles distribution of the 16 as-fabricated TMZGNR junctions. (b) STM topography images of the 16 TBZGNR junctions with twist angles ranging from 32° to 90°.



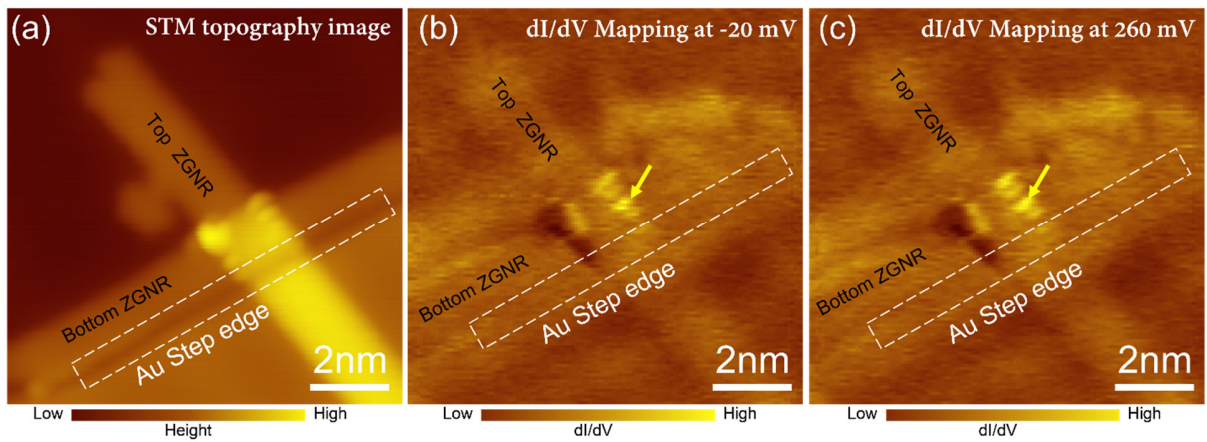
Supplementary Figure 4. Charge redistribution in the TBZGNR junction revealed by DFT calculation. (a-b) Top and side views of the charge density difference between the two overlapping ZGNRs. The charge density difference is obtained by $\rho_{\text{diff}} = \rho_{\text{total}} - \rho_{\text{top}} - \rho_{\text{bottom}}$, where ρ_{total} is the electron density of the TBZGNR, ρ_{top} and ρ_{bottom} are the electron density of only top or bottom layer ZGNR. Thus, the plots illustrate how the electrons evolve when two intrinsic ZGNRs meet. Green surfaces represent electron depletion and red surfaces represent electrons accumulation. It is clear that within the overlap region, electrons move out from the ZGNRs and accumulate in the space between them. (c) The xy-plane averaged charge density difference, where positive values mean electron gathering and negative values mean electron losing. With the help of the color shadow, one can find clearly that, spatially, in the two ZGNRs planes electrons decrease while in the middle plane electrons increase.



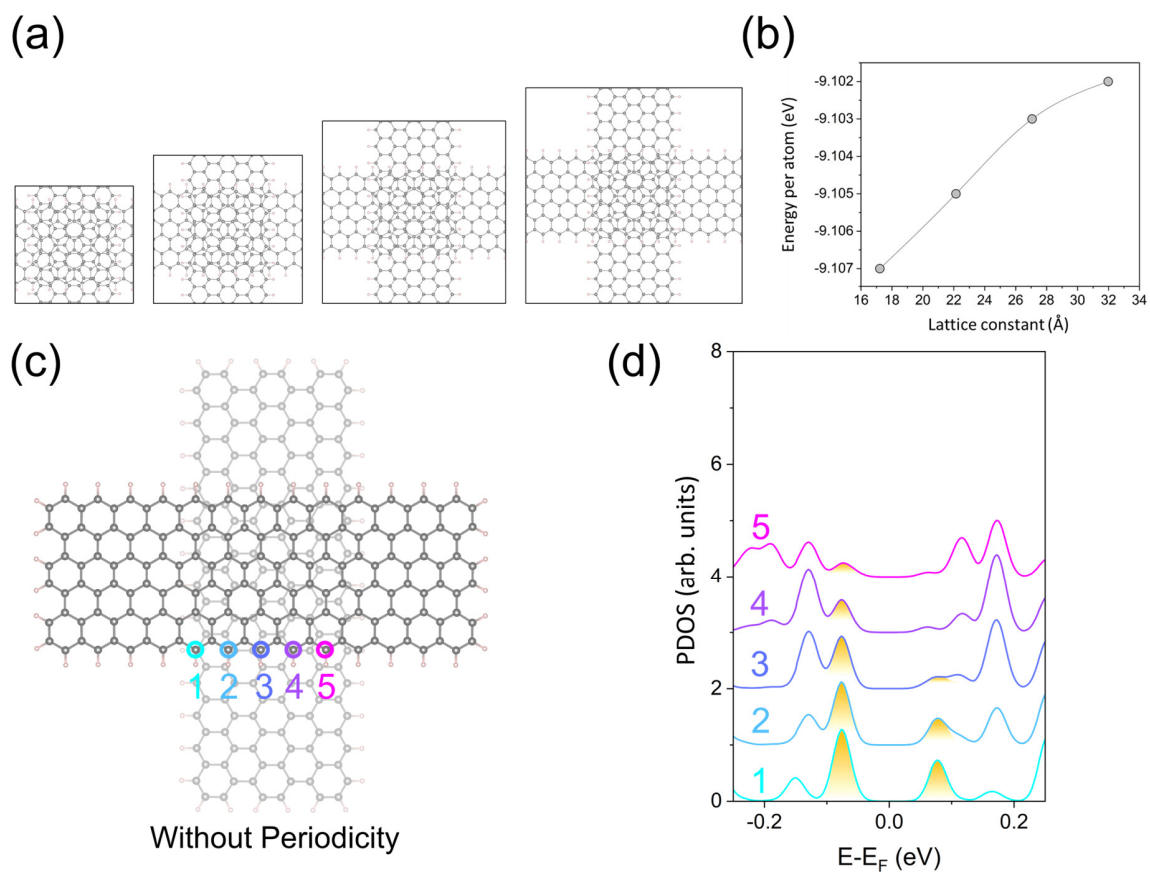
Supplementary Figure 5. DFT calculation results for another asymmetric junction model D. (a) Top view of the atomic model of another designed TBZGNR structure model D without symmetry in the overlapping area. The gray GNR is on the top. The light blue GNR is on the bottom. (b) PDOS on the edge carbon atoms labeled point 1 to point 7 in (a). The red dashed line indicates a pronounced bound state close to zero energy appears only in the regions near point 2 which is quite similar to what we calculated in model C in the main text. (c) Calculated band structure (solid lines) of the model D in (a). The solid/open circles represent projections on the left/right edge of the top GNR within the overlapping area, respectively. Blue and red colors correspond to spin up and down, respectively. One can find the spin-split bands again in this overlap region without lattice symmetry, which is similar to the case of the model C.



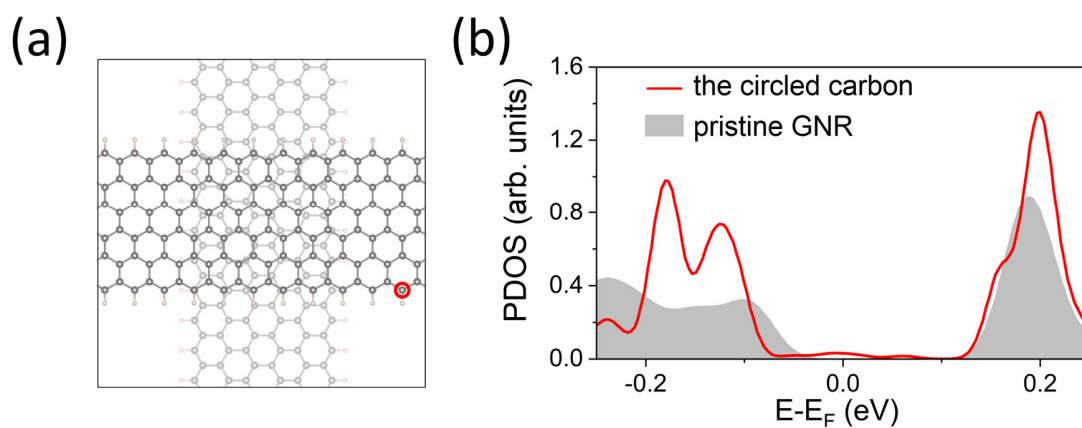
Supplementary Figure 6. STS on two TBZGNR junctions with different twist angles. (a) Topography image of the TBZGNR junction with $\theta = 32^\circ$. The white and black dashed lines indicated the edges of bottom and top ZGNR. (b) Same as (a) but the twist angle is 79° . (c) STS spectra taken on the edges of the overlap region shown in (a). Red/black spectrum recorded on the positions highlighted by the red/black dot. (d) STS spectra taken on the positions on the right edge of the TBZGNR junction indicated by the arrows. Scale bar: (a) 1 nm (b) 2 nm. Tunneling parameters: (a,b) $V = -320$ mV, $I = 1.0$ nA; (c,d) $V_{\text{stab}} = -320$ mV, $I_{\text{stab}} = 1.02$ nA



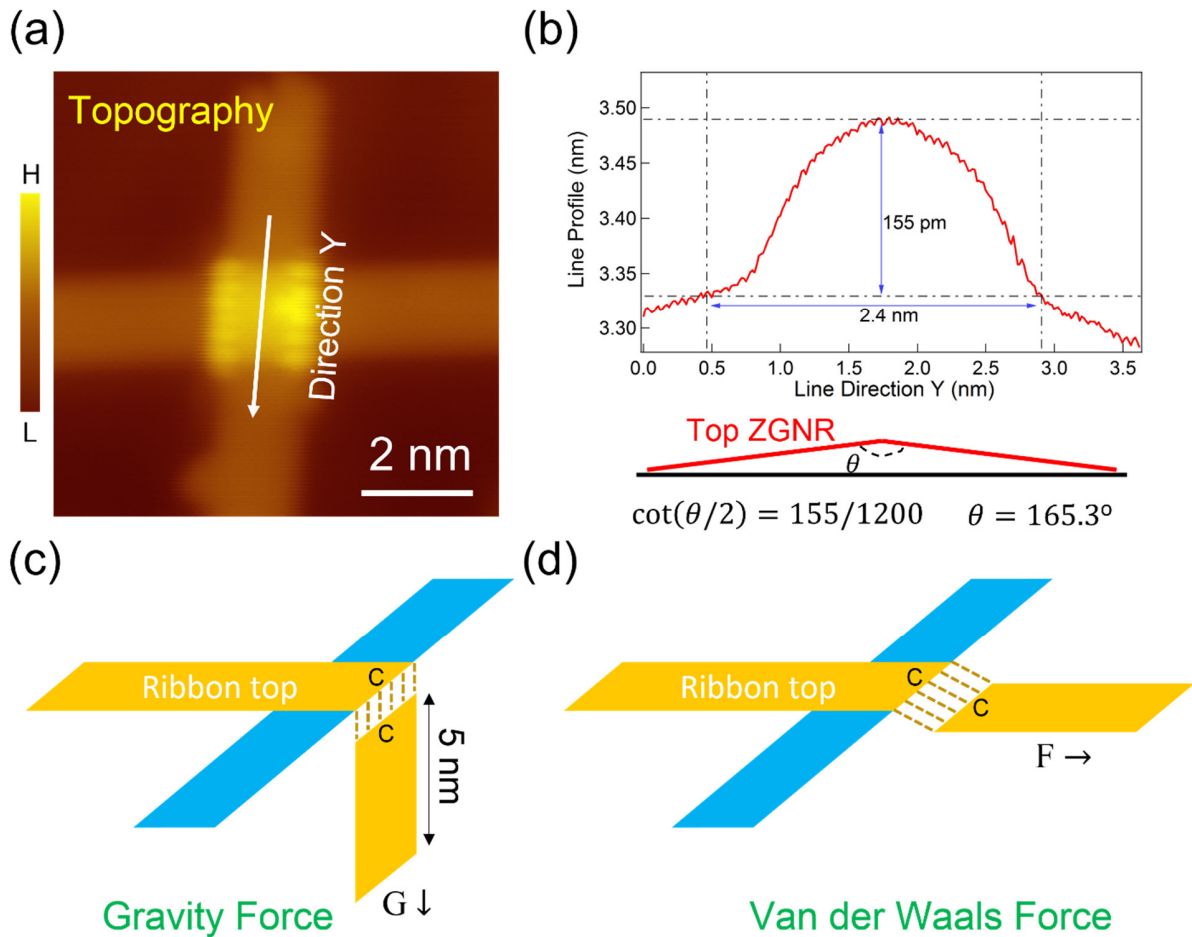
Supplementary Figure 7. dI/dV signals near the Au step edge. (a) STM topography image of one TBZGNR junction with twist angle 79° . The Au (111) step edge is highlighted with white box. (b,c) The dI/dV images of the same area at energies -20 mV and 260 mV correspondingly. The yellow arrow indicated the edge states of this TNZGNR junction.



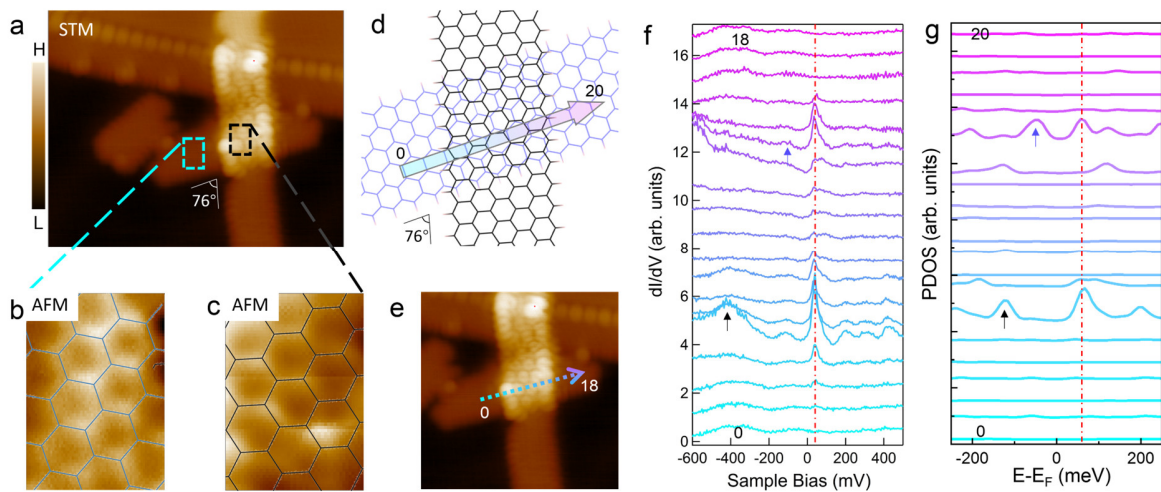
Supplementary Figure 8. DFT calculations for the TBZGNR model C under different boundary conditions. (a-b) Energy per atoms as a function of lattice constant of calculational cells. The cell sizes are 17 Å, 22 Å, 27 Å and 32 Å respectively. (c) The top view of the fragments model. The central overlapping region is the same as that in model C (Figure 3f). The five edge atoms that are projected on are highlighted with colorful circles. (d) The PDOS on the five highlighted edge atoms in (c).



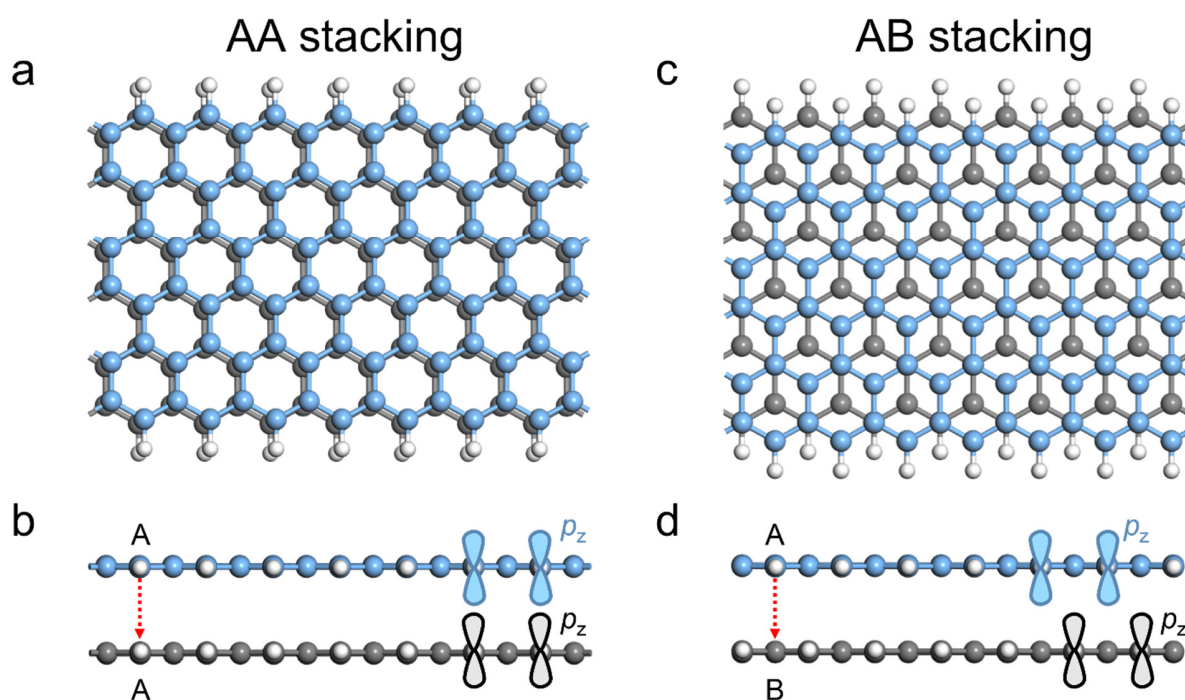
Supplementary Figure 9. DFT calculations for the monolayer ribbon edge atom close to the junction. (a) The top view of model C with a marked carbon that is off the overlapping region. (b) The projection density of state (PDOS) on the carbon in (a) (red curve) and the DOS of pristine GNR (dark shade).



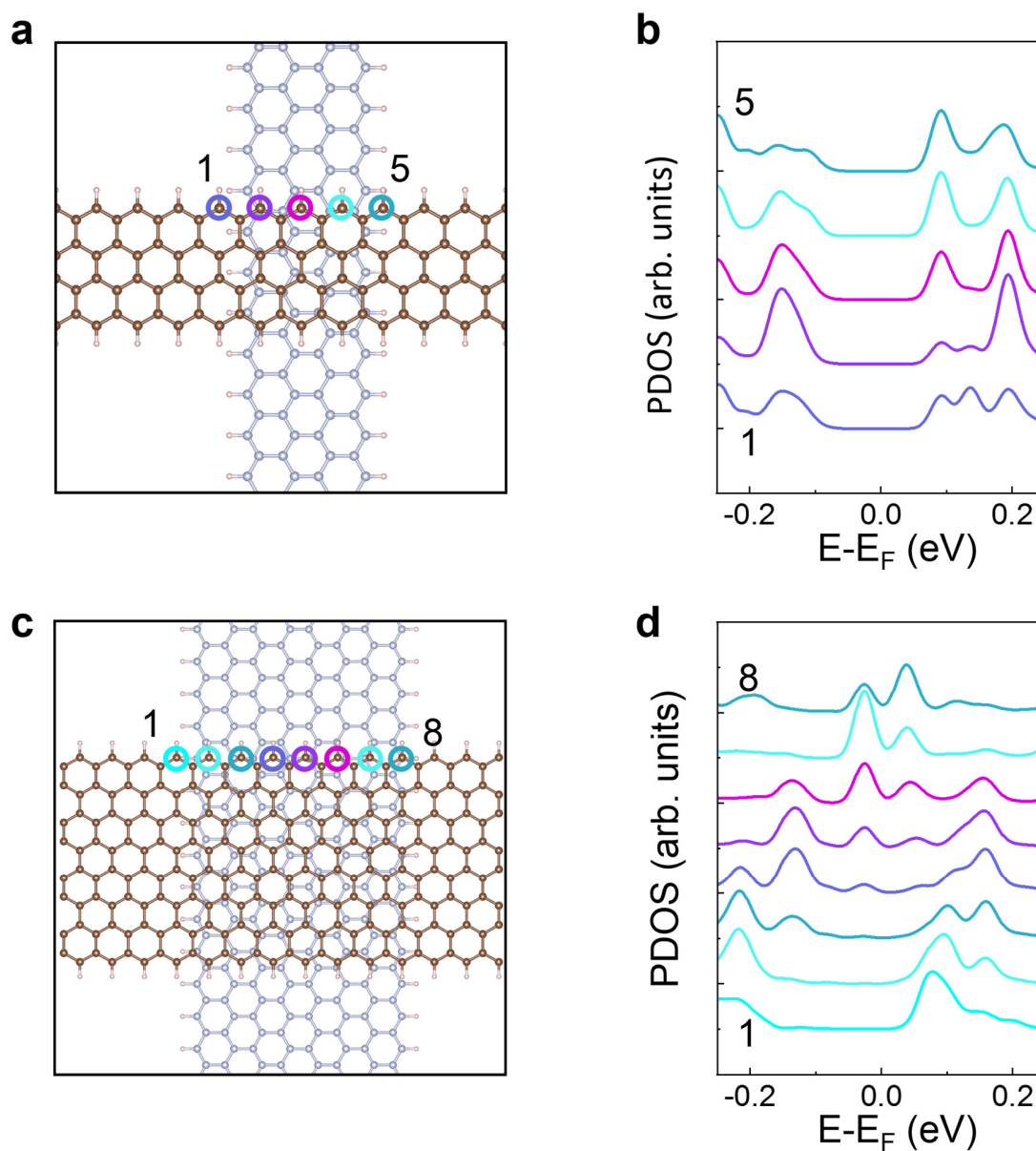
Supplementary Figure 10. Strain effect in the top layer ZGNR. (a) A replot of the STM topography image of the TBZGNR junction shown in Figure 2f. The white arrow indicates where the line profile is taken. (b) Upper panel: The line profile of the top ZGNR in the vicinity of the TBZGNR junction along the direction shown in (a). Lower panel: A simplified model plot showing the bending of the top ZGNR in the vicinity of the junction. The bending angle is 165.3° according to the data obtained in (a). (c) and (d), Schematic diagram showing local lattice distortion of the top ZGNR by only gravity force (c) and Van der Waals force (d).



Supplementary Figure 11. AFM characterization and DFT calculation on a 76° TBZGNR junction. (a) The STM image of a TBZGNR junction with a twist angle of 76°. Size 7 nm×10 nm. (b, c) Zoom-in AFM images of the bottom ZGNR (light blue) and top ZGNR (black), respectively. Size 0.7 nm×1 nm. The models are superimposed on the images. (d) TBZGNR junction with the stacking configuration obtained by extending the AFM-measured structures in (b) and (c). (e, f) 19 dI/dV spectra (f) taken across the top ribbon edges along the arrow direction shown in (e). (g) DFT calculated PDOS on 21 atoms along the path (colorful arrow) shown in model (d). The red dashed lines in (f) and (g) highlight the edge states just above Fermi energy. Tunneling parameters: (a, e) $V=-50$ mV, $I=10$ pA; (f) $V_{\text{stab}}=-50$ mV, $I_{\text{stab}}=30$ pA.



Supplementary Figure 12. Model structures for AA- and AB-stacking bilayer ZGNRs. (a, b) Top-view and side-view of AA-stacking bilayer GNRs geometry. (c, d) Top-view and side-view of AB-stacking bilayer GNRs geometry. Grey: bottom ribbon, Blue: Top ribbon. In the top view of the AA-stacking, the top ribbon is shifted a bit for clear visualization. The p_z orbitals of edge carbon atoms were illustrated to help recognizing the atomic stacking on the edges.



Supplementary Figure 13. DFT calculations for TBZGNR junctions with different width. Configurations and PDOS on edge atoms of 4-ZGNR (a, b) and 8-ZGNR (c, d) with twist angle of 90° . It is clear that in the 4-ZGNR there are some changes on edge states but not very pronounced, while in the 8-ZGNR the edge-states changes are much more abundant than those in 4-ZGNR and in 6-ZGNR, suggesting that the wider ZGNRs will produce more complicated overlapped configurations and more abundant edge states.

Supplementary References:

- 1 Kawai, S. *et al.* Superlubricity of graphene nanoribbons on gold surfaces. *Science* **351**, 957-961 (2016).
- 2 van der Lit, J., Jacobse, P. H., Vanmaekelbergh, D. & Swart, I. Bending and buckling of narrow armchair graphene nanoribbons via STM manipulation. *New J Phys* **17**, 053013 (2015).
- 3 Jung, J. & MacDonald, A. H. Accurate tight-binding models for the pi bands of bilayer graphene. *Phys Rev B* **89**, 035405 (2014).
- 4 Ruffieux, P. *et al.* On-surface synthesis of graphene nanoribbons with zigzag edge topology. *Nature* **531**, 489-492 (2016).
- 5 Van Der Lit, J. *et al.* Suppression of electron–vibron coupling in graphene nanoribbons contacted via a single atom. *Nature communications* **4**, 2023 (2013).
- 6 Li, Y., Zhang, W., Morgenstern, M. & Mazzarello, R. Electronic and magnetic properties of zigzag graphene nanoribbons on the (111) surface of Cu, Ag, and Au. *Physical Review Letters* **110**, 216804 (2013).
- 7 Lauwaet, K. *et al.* Resolving all atoms of an alkali halide via nanomodulation of the thin NaCl film surface using the Au (111) reconstruction. *Physical Review B* **85**, 245440 (2012).
- 8 Blackwell, R. E. *et al.* Spin splitting of dopant edge state in magnetic zigzag graphene nanoribbons. *Nature* **600**, 647-652 (2021).
- 9 Hu, X., Sun, L. & Krasheninnikov, A. V. Tuning electronic and magnetic properties of zigzag graphene nanoribbons by large-scale bending. *Applied Physics Letters* **100**, 263115 (2012).
- 10 Levy, N. *et al.* Strain-induced pseudo–magnetic fields greater than 300 tesla in graphene nanobubbles. *Science* **329**, 544-547 (2010).
- 11 Mao, J. *et al.* Evidence of flat bands and correlated states in buckled graphene superlattices. *Nature* **584**, 215-220 (2020).
- 12 Wang, G. *et al.* Measuring interlayer shear stress in bilayer graphene. *Physical Review Letters* **119**, 036101 (2017).
- 13 Li, S.-Y., Su, Y., Ren, Y.-N. & He, L. Valley polarization and inversion in strained graphene via pseudo-Landau levels, valley splitting of real Landau levels, and confined states. *Physical Review Letters* **124**, 106802 (2020).